J. Fluid Mech. (2021), *vol*. 919, A27, doi:10.1017/jfm.2021.385

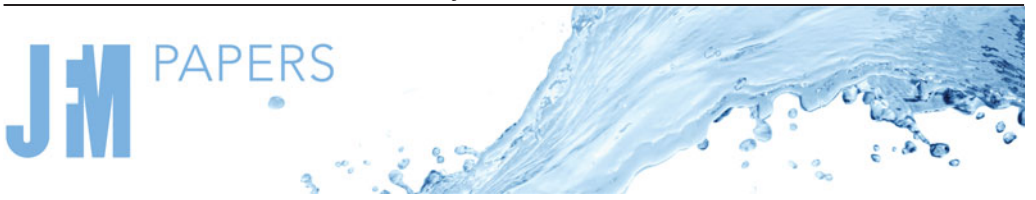

Vortex dynamics for flow around the slat cove at low Reynolds numbers

Jiang-Sheng Wang[1] **and Jin-Jun Wang**[1],†

[1]Fluid Mechanics Key Laboratory of Education Ministry, Beijing University of Aeronautics and Astronautics, Beijing 100191, China

(Received 4 June 2020; revised 20 April 2021; accepted 27 April 2021)

Time-resolved particle image velocimetry (TR-PIV) is employed to investigate the vortex dynamics around the slat cove of a 30P30N multi-element airfoil at a fixed geometric angle of attack of 4 ° within the stowed chord Reynolds number range of $9.3 \times 10^3 \leq Re_c \leq 5.2 \times 10^4$. The results link the frequency properties to the vortex shedding patterns of the slat cusp shear layer. With increasing Re_c, three types of vortex dynamics are identified: (i) no vortex shedding from the slat cusp shear layer and the absence of hydrodynamic feedback in the slat cove ($9.3 \times 10^3 \leq Re_c \leq 1.27 \times 10^4$); (ii) impingement of shed vortices on the underside of the slat trailing edge at a steady location ($1.38 \times 10^4 \leq Re_c \leq 1.83 \times 10^4$); (iii) impingement of shed vortices on the underside of the slat trailing edge at unsteady locations ($2.41 \times 10^4 \leq Re_c \leq 5.2 \times 10^4$). The fluctuations generated by shed vortices link the slat cusp and trailing edge by the hydrodynamic feedback in the slat cove. Besides the fundamental frequency and its harmonics, subharmonics and fractional harmonics occur to the slat cusp shear layer in the Re_c range of 2.41×10^4–5.2×10^4. Subharmonics make the impingement locations of shed vortices unsteady. Fractional harmonics trigger the secondary instability of the braid region between two consecutive vortices to generate more shed vortices. The vortex dynamics in this Re_c range is found to persist to $Re_c \sim 10^6$.

Key words: vortex interactions, vortex dynamics, vortex shedding

1. Introduction

As traditional high-lift systems, multi-element airfoils are extensively employed in the designs of transport aircrafts. At $Re_c = 10^6$–10^7, this kind of configuration is capable of improving the take-off and landing properties by postponing the stall and enhancing the maximum lift coefficient (Van Dam 2002). However, the slat is a large contributor to the airframe noise (Dobrzynski 2010) and can generate complex disturbances that interact

† Email address for correspondence: jjwang@buaa.edu.cn

with the boundary layer of the main element (Agoropoulos & Squire 1988; Squire 1989). As a result, progress in the vortex dynamics of slat is significant for the fundamental aspects of fluid mechanics, e.g., noise radiation and wake/boundary layer interactions. The present work is therefore focused on the flow around the slat cove to promote the physical understanding of the vortex dynamics of the slat.

Jenkins, Khorrami & Choudhari (2004) systematically proposed the typical vortex shedding patterns around the slat of 30P30N by two-dimensional particle image velocimetry (PIV; $Re_c = 3.64 \times 10^6$, $\alpha = 4\,°$–$8\,°$). The shed vortices of the slat cusp shear layer could be pushed through the gap between the slat and main element or entrained into the recirculation of the slat cove. The shed vortices of the former pattern could further interact with the von Kármán vortex streets of the blunt trailing edge. These vortex shedding patterns are also observed in the three-dimensional numerical simulation of DLR-F15 at $Re_c = 2.09 \times 10^6$ (Deck & Laraufie 2013). Deck & Laraufie (2013) found that the spanwise shed vortices of the slat cusp shear layer rapidly suffered from distortions and breakdowns. During the process of passing through the gap, spanwise vortices were deformed into streamwise vortices by the accelerated gap flow and further interacted with the spanwise vortices of the blunt trailing edge. The three-dimensional vortex shedding patterns of Deck & Laraufie (2013) have been verified by many numerical simulations (Choudhari & Lockard 2015; Terracol *et al*. 2015; Ashton, West & Mendonça 2016; Zhang *et al*. 2017). Dobrzynski (2010) mentioned that the shed vortices of the slat cusp shear layer were the sources of slat noise. Therefore, these vortex shedding patterns mentioned above should closely link to the frequency properties of slat flows.

Three typical frequency properties have been generalized from the slat noise of wind tunnel experiments ($Re_c \sim 10^6$): a broadband portion, a high-frequency hump and several narrowband peaks. Choudhari & Khorrami (2007) and Souza *et al*. (2019) found that the broadband noise could be attributed to the three-dimensional evolution of the large-scale shed vortices originating from the slat cusp shear layer. The von Kármán vortex streets of the blunt trailing edge have been found to be responsible for the high-frequency hump (Khorrami, Berkman & Choudhari 2000; Olson, Thomas & Nelson 2001; Terracol *et al*. 2015). It is accepted that the narrowband peaks are ascribed to the aeroacoustic feedback within the slat cove (Deck & Laraufie 2013; Terracol *et al*. 2015; Pascioni & Cattafesta 2018*b*; Souza *et al*. 2019). This aeroacoustic feedback is similar to the Rossiter-mode of cavity flow (Rossiter 1964). Terracol *et al*. (2015) have successfully predicted these narrowband peaks by an improved Rossiter equation. Similar to the mode-switching of cavity flow (Kegerise *et al*. 2004), Li *et al*. (2018*a*) observed that these narrowband peaks were intermittently excited in the far-field noise spectra. Notably, Dobrzynski (2010) mentioned that narrowband peaks could be a consequence of low Reynolds numbers ($Re_c \sim 10^6$) in massive investigations and absent at $Re_c \sim 10^7$ (full scale of aircraft). Pott-Pollenske, Delfs & Reichenberger (2013) also reported that the slat noise spectra at $Re_c = 5 \times 10^6$ did not contain any narrowband peaks. However, Lockard & Choudhari (2012) and Herr *et al*. (2015) found that narrowband peaks robustly existed in the slat noise spectra at $Re_c = 1.2 \times 10^7$ and at $Re_c = 5 \times 10^6$, respectively. Although whether narrowband peaks exist in the slat noise spectra at $Re_c \sim 10^7$ is an open question, massive benchmark investigations captured narrowband peaks in the slat noise spectra at $Re_c \sim 10^6$ (Murayama *et al*. 2014; Choudhari & Lockard 2015; Li *et al*. 2017, 2018*a*; Pascioni & Cattafesta 2018*a*). The flow physics behind these narrowband peaks is therefore an important topic for fundamental research. Recently, Souza *et al*. (2019) linked these narrowband peaks to the large-scale shed vortices of the slat cusp shear layer. As the large-scale shed vortices impinged on the underside of slat trailing edge, sound waves were emitted and convected to the slat cusp for disturbing the free shear layer (Souza *et al*. 2019).

However, the specific vortex shedding patterns of different narrowband peaks still need further explorations.

The effects of α and Re_c ($Re_c = 8.32 \times 10^3$–3.05×10^4, $\alpha = 0\,°$–$16\,°$) on the vortex dynamics of a 30P30N multi-element airfoil have been investigated at low Reynolds numbers (Wang *et al.* 2018, 2019). When $Re_c = 8.32 \times 10^3$, the upper right boundary of the slat cove recirculation worked as a virtual curved wall to generate centrifugal instability, which led to Görtler vortices in the slat wake ($\alpha = 2\,°$–$12\,°$). For a fixed α of $4\,°$, the dominated vortices in the slat wake changed from Görtler vortices to spanwise shed vortices with the increase of Re_c from 8.32×10^3 to 3.05×10^4, which unveiled a critical Re_c interval of 1.27×10^4–1.38×10^4 for this change. However, Wang *et al.* (2018, 2019) mainly focused on the wake/shear layer interactions over the main element. The vortex dynamics around the slat at low Reynolds numbers still requires further investigations, which may also reveal the links of slat flows between low and high Reynolds numbers.

The current work is motivated by the need for an improved understanding of the vortex dynamics around the slat. With time-resolved PIV (TR-PIV), the vortex dynamics around the slat of a 30P30N airfoil is investigated with a fixed geometric α of $4\,°$ within the Reynolds number range of $9.3 \times 10^3 \leq Re_c \leq 5.2 \times 10^4$. The uniqueness lies on the detailed links between the different vortex shedding patterns of the slat cusp shear layer and the narrowband peaks of slat flows. To the best of the authors' knowledge, such specific links have not been reported before. It will be shown that the vortex dynamics in the range of $2.41 \times 10^4 \leq Re_c \leq 5.2 \times 10^4$ could be correlated with that of $Re_c \sim 10^6$, which promotes the physical understanding for the vortex dynamics of a slat at $Re_c \sim 10^6$. The paper is structured as follows: § 2 describes the experimental set-up and post-processing tools; the effects of Re_c on the typical characteristics of mean flow statistics are presented in § 3; in § 4, the effects of Re_c on the vortex dynamics are discussed in detail; the evidence of close links in vortex dynamics between $2.41 \times 10^4 \leq Re_c \leq 5.2 \times 10^4$ and $Re_c \sim 10^6$ is provided in § 5; the main conclusions are given in § 6.

2. Experimental methodology

2.1. *Experimental set-up*

Experiments were performed in the water tunnel of the Institute of Fluid Mechanics at the Beijing University of Aeronautics and Astronautics, which has a test section of $600 \times 600 \times 3000$ mm (height × width × length). The free stream turbulence intensities were no more than 0.8 % for all the test cases. The current 30P30N multi-element airfoil is a scaled model of AIAA BANC-II Workshop (Choudhari & Lockard 2015). It has a stowed chord length (c) of 150 mm and an aspect ratio of 3.33. The slat has a chord length ($c_s = 15\,\%c$) of 22.5 mm. The aspect ratio (Jenkins *et al.* 2004; Pascioni & Cattafesta 2018*b*) and the circular endplates at two sides of the airfoil (Boutilier & Yarusevych 2012) guarantee a quasi-two-dimensional mean flow around the mid-span region of the airfoil (Wang *et al.* 2019). Therefore, the wall effects on the flow physics discussed in the current work were negligible. No boundary layer trip was used. The geometric angle of attack, defined as the angle between the chord line of the clean configuration and the inflow direction, was fixed at $4\,°$. Notably, the high camber and the strong circulation of the multi-element airfoil induced high-flow deflection, which led to evident deviations between the geometric and the effective angles of attack in the measurement with an open-jet wind tunnel (Murayama *et al.* 2014; Manoha & Pott-Pollenske 2015; Li *et al.* 2017; Jawahar *et al.* 2020). Normally, the geometric angle of attack is shifted to an

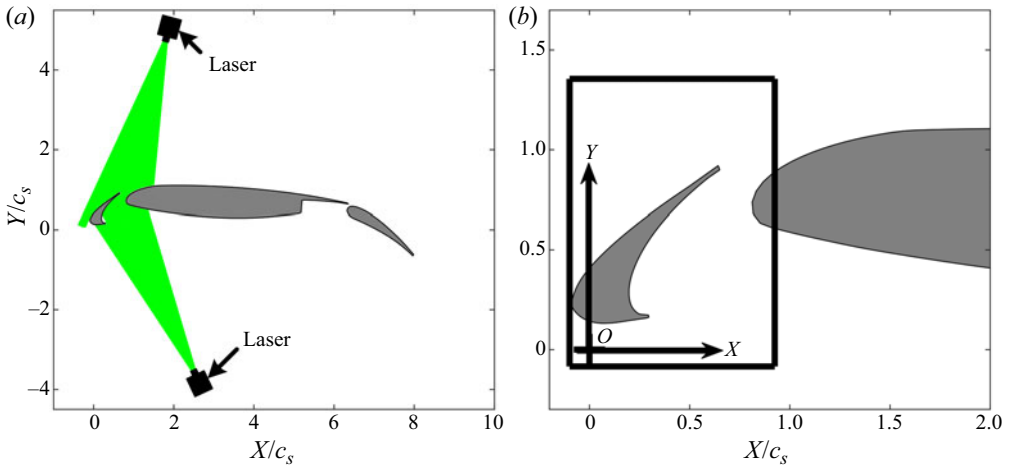

Figure 1. Experimental set-up. The distances between the lasers and the airfoil are longer than those sketched in (*a*). The field of view of TR-PIV measurements is sketched by the black box in (*b*).

effective angle of attack according to the pressure distributions above the multi-element airfoil (Murayama *et al*. 2014; Pascioni & Cattafesta 2018*b*; Jawahar *et al*. 2020). Because the current experimental set-up was designed to be focused on the evolutions of flow structures in a water tunnel, the pressure distributions above the multi-element airfoil were unavailable and therefore no aerodynamic correction was applied to the current results. Accordingly, an effective angle of attack was unavailable in the current work. Li *et al*. (2017) has shown that the pressure distribution and flow field of a 30P30N configuration in a closed hard-wall wind tunnel are comparable to those in ideal free flight conditions. Therefore, the deviations between the geometric and the effective angles of attack of the multi-element airfoil are alleviated in the measurement with a closed hard-wall wind tunnel. The current experiments were performed in a water tunnel, comparable to those performed in a closed hard-wall wind tunnel. Therefore, it could be deduced that the current effective angle of attack was still approximately 4 °. The origin of the coordinate system (O in figure 1) was located at the leading edge of the slat at $\alpha = 0\,°$, consistent with Wang *et al*. (2018, 2019). X and Y denote the streamwise and vertical directions, respectively. As the free stream velocity U_∞ varied from 62 to 348 mm s^{-1}, the Reynolds number based on c (Re_c) varied from 9.3×10^3 to 5.2×10^4. More details of the model design and related water tunnel can be found in the papers by Wang *et al*. (2018, 2019).

Two-dimensional TR-PIV was used to measure the flow around the slat cove. The flow was seeded with hollow glass beads with a median diameter of 10 μm. Two semiconductor continuous lasers (8 W, 532 nm) were co-operated to illuminate the gap region between the slat and the main element, by aligning the two laser sheets (thickness of ∼1 mm) to one plane (figure 1*a*). PIV images were captured by a Photron FASTCAM SA2 high-speed CMOS camera with a TAMRON lens (focal length of 90 mm). The field of view was fixed as 23 mm × 32 mm (sketched by a black box in figure 1(*b*)). The shutter time of the CMOS camera equalled $1/f_s$, where f_s is the sampling frequency of the CMOS camera. An increase of Re_c from 9.3×10^3 to 5.2×10^4 led to an increase of f_s from 250 to 1500 Hz. The magnification was fixed as 0.035 mm pix^{-1}. The velocity fields were

calculated by the multi-pass iterative Lucas–Kanade algorithm (MILK algorithm) with a final interrogation window of 32×32 pixels and an overlap of 75 %, which led to a spatial resolution of $0.05c_s$ and a vector pitch of $0.0125c_s$. This algorithm is based on the sum of square difference (SSD) optimization and can provide dense velocity fields with relatively fewer outliers. More details of the MILK algorithm can be found in the papers by Champagnat *et al*. (2011) and Pan *et al*. (2015). The statistical estimations contained at least 12 585 PIV snapshots. Following the strategies of Qu *et al*. (2019), the instantaneous velocity uncertainties relative to the free stream velocities in all PIV measurements were estimated to be less than 1.6 %. The uncertainties of spanwise vorticity (normalized by dividing U_∞/c_s) were estimated to be less than 0.93. The uncertainties of two-dimensional turbulent kinetic energy were estimated to be less than $0.09\,\%U_\infty^2$.

2.2. *Post-processing tools*

2.2.1. *Finite-time Lyapunov exponents method*

Finite-time Lyapunov exponents (FTLEs) characterize the maximum exponential divergence of nearby fluid trajectories within a finite time interval (Haller & Yuan 2000; Haller 2001; Shadden, Dabiri & Marsden 2006). The FTLE ridges are defined as the concentrated region of FTLEs and can be used to extract Lagrangian coherent structures (LCSs). The LCSs with attracting properties will be obtained by backward integrating the fluid trajectories based on the velocity fields of TR-PIV (He *et al*. 2016; Wang *et al*. 2018). In the current work, the FTLEs method was employed to extract LCSs of the slat cusp shear layer. The time interval used for the computation of FTLEs was longer than six vortex shedding cycles related to the fundamental frequency at each case. Notably, no vortex shedding occurred to the slat cusp shear layer at $Re_c = 1.27 \times 10^4$. The time interval for the computation of FTLEs at $Re_c = 1.27 \times 10^4$ was therefore chosen as a value comparable to that at $Re_c = 1.38 \times 10^4$.

2.2.2. *Wavelet analysis*

The continuous wavelet transform (CWT) can provide the joint time-frequency properties of signals (Mallat 1999). It has been successfully employed to reveal the transient properties of slat noise signals (Li *et al*. 2018*a*; Jawahar *et al*. 2020). The CWT is defined as

$$W_x(a, \tau) = \int_{-\infty}^{+\infty} x(t)\Psi^*_{a,\tau}(t)\,\mathrm{d}t, \tag{2.1}$$

where $W_x(a,\tau)$ is the wavelet coefficient of signal $x(t)$, $\Psi_{a,\tau}(t)$ is the wavelet function, * denotes the complex conjugate, a is the wavelet scale and τ is the wavelet time delay. $\Psi_{a,\tau}(t)$ is defined as

$$\Psi_{a,\tau}(t) = a^{-1/2}\Psi\left(\frac{t-\tau}{a}\right). \tag{2.2}$$

Li *et al*. (2018*a*) found that a Morlet wavelet (Morlet 1983) was superior in revealing the transient properties of narrowband peaks. Because the narrowband peaks could correlate with the vortex dynamics of the slat cusp shear layer (Souza *et al*. 2019), the current work also employed CWT with a Morlet wavelet to unveil the transient properties of the vortices shedding from the slat cusp shear layer. Similar to Wang *et al*. (2019), the fluctuation signals $x(t)$ only contained the components vertical to the main flow directions (v^{tran}),

which reduced the effects of varied main flow directions on $x(t)$ and increased the relevance between $x(t)$ and the shed vortices. The Morlet wavelet is defined as

$$\Psi(t) = \mathrm{e}^{\mathrm{i}\omega_0 t}\,\mathrm{e}^{-t^2/2}, \tag{2.3}$$

where ω_0 is the non-dimensional frequency and is usually chosen as 6 for satisfying the admissibility condition (Farge 1992). Notably, the v^{tran} signals used for the current wavelet analyses contain at least 210 vortex shedding cycles related to the fundamental frequency at each case.

2.2.3. *Fluctuation reconstructions*

Different vortex shedding patterns of the slat cusp shear layer produce fluctuations with different frequency properties. Fluctuation reconstructions within different frequency bands could shed more light on the vortex dynamics of the slat cusp shear layer. After applying single-point discrete Fourier transformation to every fluctuation sequence within the field of view, a Fourier-transform matrix ($\boldsymbol{c_k}$) is obtained:

$$\boldsymbol{c_k} = \frac{1}{N}\sum_{n=0}^{N-1} \boldsymbol{F_n}\,\mathrm{e}^{-\mathrm{i}(2\pi k/N)n}, \tag{2.4}$$

where N and $\boldsymbol{F_n}$ denote the total sampling number and the matrix of fluctuation sequences, respectively. The fluctuations within different frequency bands ($\boldsymbol{F_n^{band}}$) are then reconstructed by applying inverse Fourier transformation to $\boldsymbol{c_k}$:

$$\boldsymbol{F_n^{band}} = \sum_{band} \boldsymbol{c_k}\,\mathrm{e}^{\mathrm{i}(2\pi k/N)n}. \tag{2.5}$$

As mentioned in § 2.2.2, only v^{tran} is contained in $\boldsymbol{F_n}$. In addition, the sampling time of $\boldsymbol{F_n}$ used for the current fluctuation reconstructions contains at least 210 vortex shedding cycles related to the fundamental frequency at each case.

3. Typical characteristics of mean flow statistics

In this section, the effects of Re_c on the typical characteristics of mean flow statistics, which include the topology in the slat cove, the reattachment locations of the slat cusp shear layer on the underside of slat trailing edge and the two-dimensional turbulent kinetic energy in the slat cusp shear layer, are discussed. These typical characteristics contribute to an overview of the current slat flows and provide references to the analyses of vortex dynamics in § 4.

The time-averaged vorticity contours superimposed with related streamlines are presented in figure 2. As Re_c is increased, the recirculation between the slat cusp shear layer and the slat cove shrinks in the streamwise direction. Meanwhile, the reattachment location where the slat cusp shear layer impinges on the underside of trailing edge (marked by the red dot in figure 2) moves away from the trailing edge. Two distinct patterns are captured in the current Re_c range: (i) when $Re_c \leq 3.05 \times 10^4$, the main recirculation and the small counter-rotating recirculation (secondary recirculation) result in a double-recirculation pattern in the slat cove (figure 2*a–f*); (ii) when $Re_c \geq 4.61 \times 10^4$, the secondary recirculation vanishes, which leads to a single-recirculation pattern in the slat cove (figure 2*g–h*). The single-recirculation pattern after $Re_c = 4.61 \times 10^4$ is consistent with the topology at $Re_c \sim 10^6$ (Jenkins *et al.* 2004; Pascioni, Cattafesta &

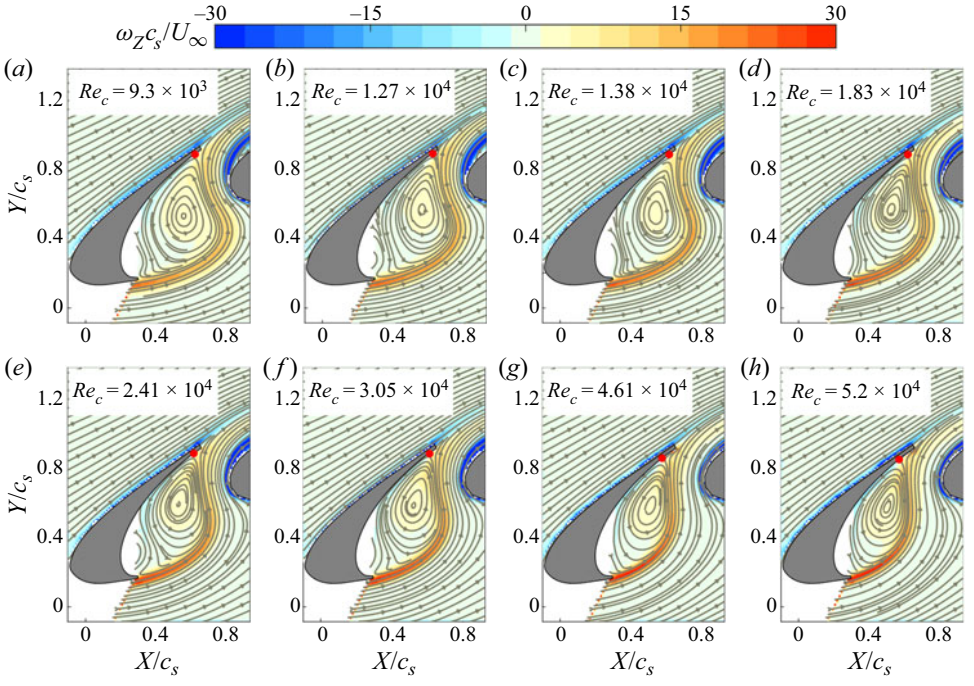

Figure 2. Mean vorticity contours with the superimposition of streamlines: (*a*) $Re_c = 9.3 \times 10^3$; (*b*) $Re_c = 1.27 \times 10^4$; (*c*) $Re_c = 1.38 \times 10^4$; (*d*) $Re_c = 1.83 \times 10^4$; (*e*) $Re_c = 2.41 \times 10^4$; (*f*) $Re_c = 3.05 \times 10^4$; (*g*) $Re_c = 4.61 \times 10^4$; (*h*) $Re_c = 5.2 \times 10^4$. The red dots mark the impingement locations of the slat cusp shear layer on the underside of the tailing edge. Although the mean vorticity contours in (*b*) and (*d*) have been reported by Wang *et al*. (2018), it is still relevant to show them here for an integrated illustration of the effects of Re_c on the mean flow statistics.

Choudhari 2014). In addition, the distance between the slat trailing edge and the reattachment location is estimated to be $0.1c_s$ at $Re_c = 5.2 \times 10^4$, which is consistent with the estimation of Jenkins *et al*. (2004) at $Re_c = 3.64 \times 10^6$. Strong two-dimensional turbulent kinetic energy (k/U_∞^2) exists within the slat cusp shear layer after $Re_c = 1.38 \times 10^4$ (figure 3), which is consistent with the occurrence of vortex shedding after $Re_c = 1.38 \times 10^4$ (Wang *et al*. 2019). As Re_c increases, a marked increase of k/U_∞^2 is observed within the slat cusp shear layer. It should be mentioned that five virtual probes are defined at the local peaks of k/U_∞^2 (magenta crosses in figure 3) for characterizing the frequency properties of the slat cusp shear layer in § 4.

4. Vortex dynamics

In this section, the effects of Re_c on the vortex dynamics around the slat are presented. It is found that three types of vortex dynamics occur to the slat cusp shear layer: (i) absence of vortex shedding ($9.3 \times 10^3 \leq Re_c \leq 1.27 \times 10^4$); (ii) impingement of shed vortices on the underside of the slat trailing edge at a steady location ($1.38 \times 10^4 \leq Re_c \leq 1.83 \times 10^4$); (iii) impingement of shed vortices on the underside of slat trailing edge at unsteady locations ($2.41 \times 10^4 \leq Re_c \leq 5.2 \times 10^4$). The typical LCSs and their links to the spectral properties in each type of vortex dynamics will be discussed in detail.

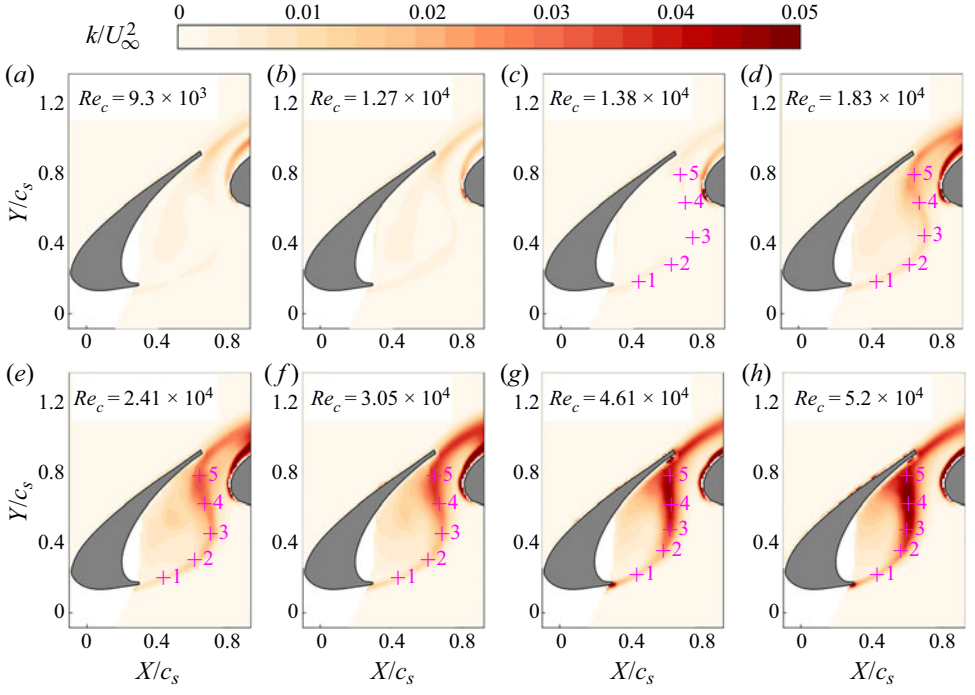

Figure 3. Two-dimensional turbulent kinetic energy contours (k/U_∞^2): (*a*) $Re_c = 9.3 \times 10^3$; (*b*) $Re_c = 1.27 \times 10^4$; (*c*) $Re_c = 1.38 \times 10^4$; (*d*) $Re_c = 1.83 \times 10^4$; (*e*) $Re_c = 2.41 \times 10^4$; (*f*) $Re_c = 3.05 \times 10^4$; (*g*) $Re_c = 4.61 \times 10^4$; (*h*) $Re_c = 5.2 \times 10^4$. The magenta crosses are located at the local peaks of k/U_∞^2. The fluctuations vertical to the main flow directions (v^{tran}) are extracted from these crosses to calculate the spectra in the current work.

4.1. *Absence of vortex shedding*

The LCSs of the typical case of $Re_c = 1.27 \times 10^4$ are shown in figure 4(*a–d*). Consistent with Wang *et al.* (2019), no vortex shedding occurs to the slat cusp shear layer when $Re_c \leq 1.27 \times 10^4$. The absence of vortex shedding leads to no obvious fluctuation around the reattachment location of the slat cusp shear layer. As a result, there is no obvious correlation between the reattachment location and the initial free shear layer around the slat cusp. In contrast, at $Re_c = 1.38 \times 10^4$, the spanwise shed vortex of the slat cusp shear layer (V_S in figure 4(*e–h*)) will impinge on the underside of the slat trailing edge and subsequently be cut into two parts by the trailing edge: one part passes through the gap region and is convected downstream; the other part is entrained into the recirculation as a vortex fluctuation (V_D in figure 4(*e–h*)). V_D will be convected by the recirculation to the slat cusp and further disturb the free shear layer. Consequently, a hydrodynamic feedback links the slat cusp and trailing edge. The vortex dynamics at $Re_c = 1.38 \times 10^4$ will be further discussed in the next subsection.

4.2. *Impingement of shed vortices on the underside of the trailing edge at a steady location*

Vortex shedding occurs to the slat cusp shear layer when $Re_c \geq 1.38 \times 10^4$ (Wang *et al.* 2019). Welch's method (Welch 1967) is applied to the v^{tran} signals at the probes 1–5 of figure 3(*c*,*d*) to estimate the spectral properties of the slat cusp shear layer,

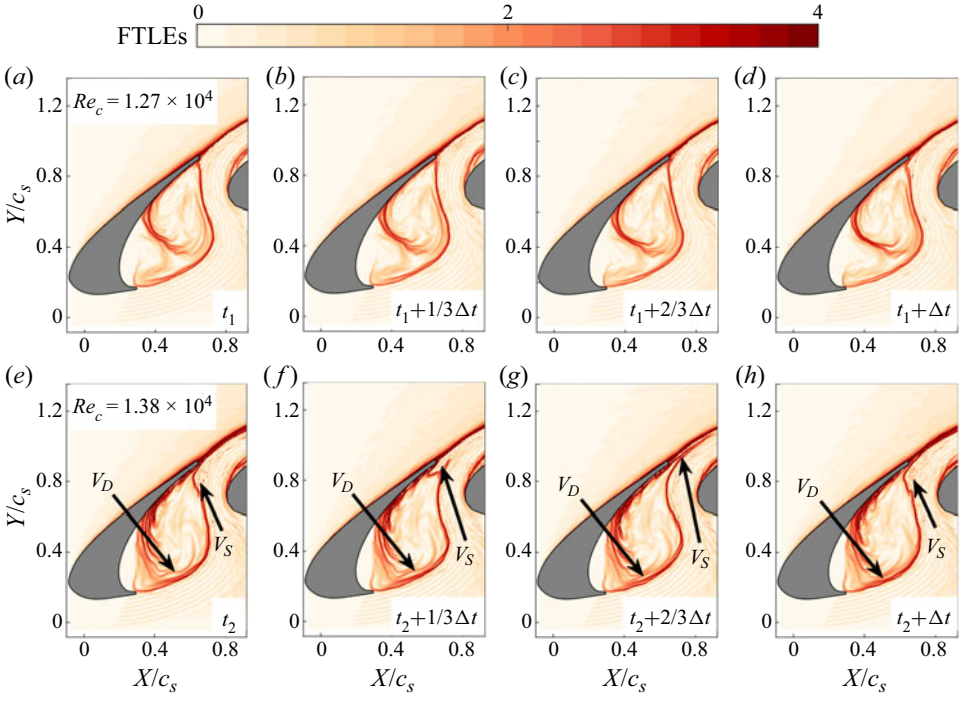

Figure 4. The LCSs revealed by the FTLEs method: (*a–d*) $Re_c = 1.27 \times 10^4$; (*e–h*) $Re_c = 1.38 \times 10^4$. Here, V_S denotes the shed vortex of the slat cusp shear layer; V_D denotes the vortex fluctuation produced by the impingement of V_S on the underside of the trailing edge; and Δt is chosen as the shedding period of V_S.

which effectively reduces the effects of noise. The v^{tran} signal is first divided into 10 blocks with a 75 % overlapping Hanning window, which leads to 3595 data points in each block. The v^{tran} signal in each block is then transferred into a power spectral density by a fast Fourier transform. The power spectral densities of these 10 blocks are finally averaged to provide the power spectral densities in figure 5, which leads to a frequency resolution of $1/3595 f_s$ (f_s is the sampling frequency of the CMOS camera). Figure 5 demonstrates the dominance of the fundamental frequency (St_1) and second harmonic (St_2) for $1.38 \times 10^4 \leq Re_c \leq 1.83 \times 10^4$. The similar power spectral densities in figure 5(*a*,*b*) indicate the similar vortex dynamics of $1.38 \times 10^4 \leq Re_c \leq 1.83 \times 10^4$. As mentioned by Wang *et al*. (2019), the formations and deformations of the shed vortices could be related to St_1 and St_2, respectively. At the early stage of the slat cusp shear layer (probe 1 in figure 5), only St_1 is remarkable. As the vortex shedding occurs, St_2 appears in the slat cusp shear layer (at probe 4 in figure 5(*a*) and probe 2 in figure 5(*b*)). Because the probes marked by the same number in figure 3 are located at similar vertical positions, figure 5 reveals the upstream move (to the slat cusp) of St_2 with increasing Re_c, coupled with the upstream move of vortex shedding (Wang *et al*. 2019). In addition, the stronger shed vortices at $Re_c = 1.83 \times 10^4$ (owing to higher Re_c) lead to the stronger fundamental frequency and harmonics in figure 5(*b*) than those in figure 5(*a*). Notably, the PIV measurements at each Reynolds number are repeated three times to ensure the repeatability and reliability of the frequency peaks in figure 5.

Figure 6 shows the wavelet spectra of the v^{tran} signals around the impingement location ($1.38 \times 10^4 \leq Re_c \leq 1.83 \times 10^4$). The dominant St_1 persists over the time interval, which

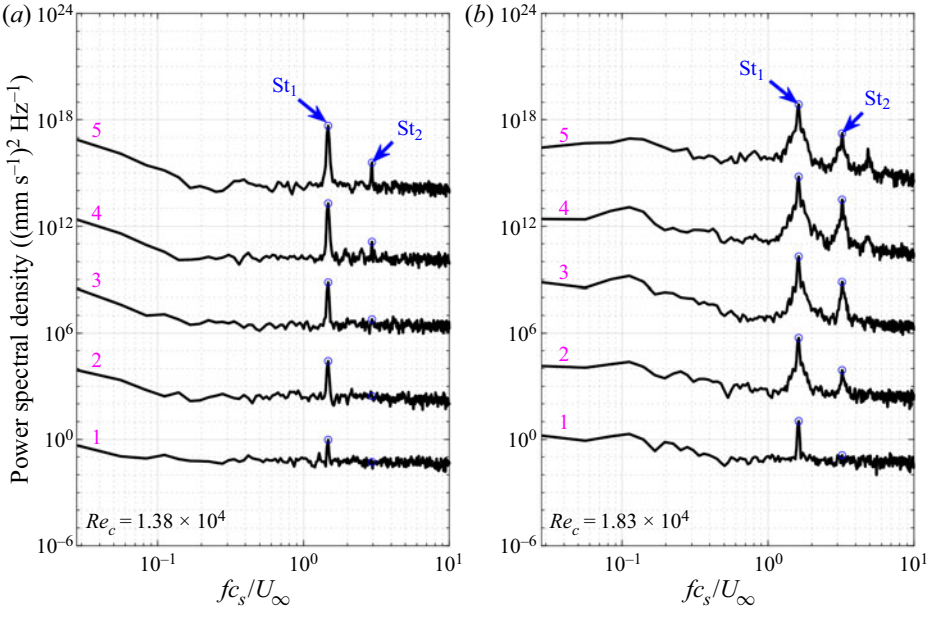

Figure 5. Power spectral densities in the slat cusp shear layer: (*a*) $Re_c = 1.38 \times 10^4$; (*b*) $Re_c = 1.83 \times 10^4$. The local power spectral densities of 1–5 are calculated from the v^{tran} signals at the probes 1–5 of figure 3, respectively. St_1 and St_2 denote the fundamental frequency and second harmonic, respectively. The power spectral densities of each subfigure are amplified step by step by 10^4 along the probe positions for clarity.

indicates a good periodicity for the impingement of shed vortices on the underside of the trailing edge. The LCSs at $Re_c = 1.38 \times 10^4$ (figure 4*e–h*) and $Re_c = 1.83 \times 10^4$ (figure 7) further verify the good periodicity of the impingement. Similar to the case of $Re_c = 1.38 \times 10^4$, the vortex fluctuation (V_D in figure 7) links the slat cusp and trailing edge by a hydrodynamic feedback.

4.3. *Impingement of shed vortices on the underside of the trailing edge at unsteady locations*

When $2.41 \times 10^4 \leq Re_c \leq 5.2 \times 10^4$, the shed vortices of the slat cusp shear layer impinge on the underside of the trailing edge with unsteady impingement locations. Similar to the strategy of figure 5, Welch's method (Welch 1967) is applied to the v^{tran} signals at the probes 1–5 of figure 3(*e–h*) to estimate the spectral properties of the slat cusp shear layer (figure 8), which effectively reduces the effects of noise. In addition to the fundamental frequency (St_1) and its harmonics (only the second one, St_2, is marked), subharmonics ($St_{0.*}$) and fractional harmonics ($St_{1.*}$) occur to the slat cusp shear layer (figure 8). Notably, the PIV measurements at each Reynolds number are repeated three times to ensure the repeatability and reliability of the frequency peaks in figure 8, although the subharmonics in figure 8(*d*) are indeed not prominent. The 'imperfect' peaks of subharmonics could be attributed to the insufficient sampling time of the v^{tran} signals, which is limited by the camera onboard memory during the PIV measurements. However, the 'imperfect' peaks do not affect the flow physics discussed in the current work, because the vortex shedding patterns related to these 'imperfect' peaks will be captured during the sampling time (§ 4.3.4). The Strouhal numbers ($St = fc_s/U_\infty$) of $St_{0.*}$ and $St_{1.*}$ are found to be located

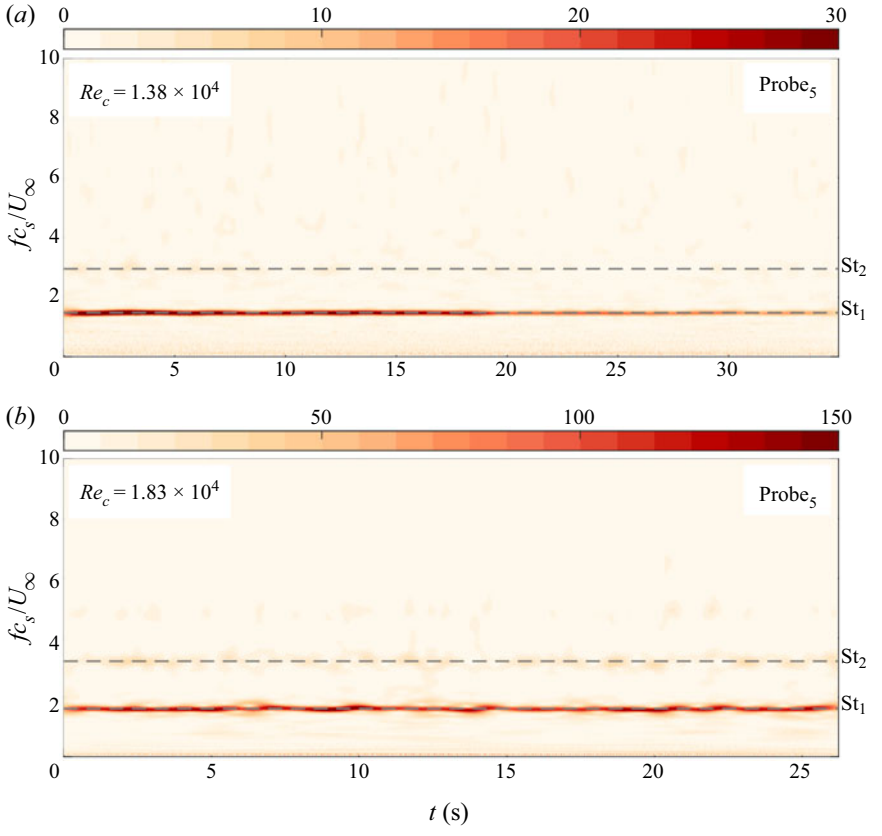

Figure 6. Wavelet spectra of the v^{tran} signals at probe 5 of figure 3: (*a*) $Re_c = 1.38 \times 10^4$; (*b*) $Re_c = 1.83 \times 10^4$. Here, St_1 and St_2 denote the fundamental frequency and second harmonic, respectively.

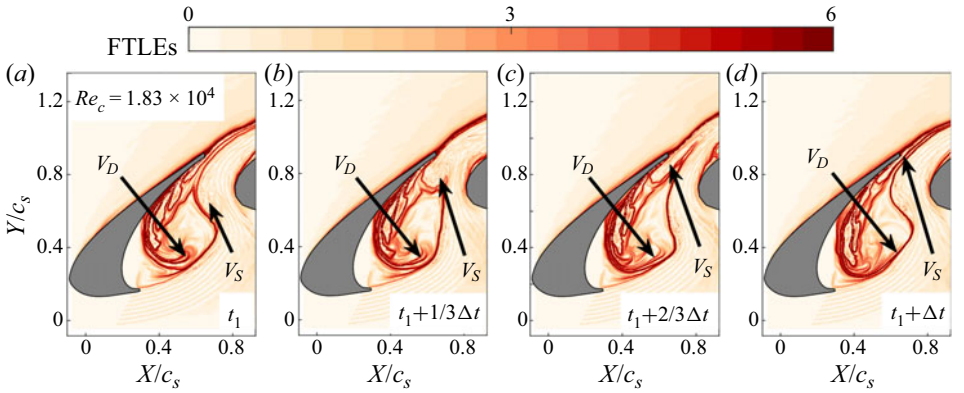

Figure 7. The LCSs revealed by the FTLEs method at $Re_c = 1.83 \times 10^4$. Here, V_S denotes the shed vortex of the slat cusp shear layer; V_D denotes the vortex fluctuation produced by the impingement of V_S on the underside of the trailing edge; and Δt is chosen as the shedding period of V_S.

around 1–5, similar to the narrowband peaks of the slat noise at $Re_c \sim 10^6$ (Murayama *et al.* 2014; Li *et al.* 2017; Pascioni & Cattafesta 2018*a*). It should be emphasized that the ratios of $St_{0.*}$ to St_1 are located around $1/3St_1$, $1/2St_1$ and $2/3St_1$, while the ratios of $St_{1.*}$ to St_1 are located around $4/3St_1$, $3/2St_1$ and $5/3St_1$. In addition to the universal law mentioned above, these subharmonics and fractional harmonics also show

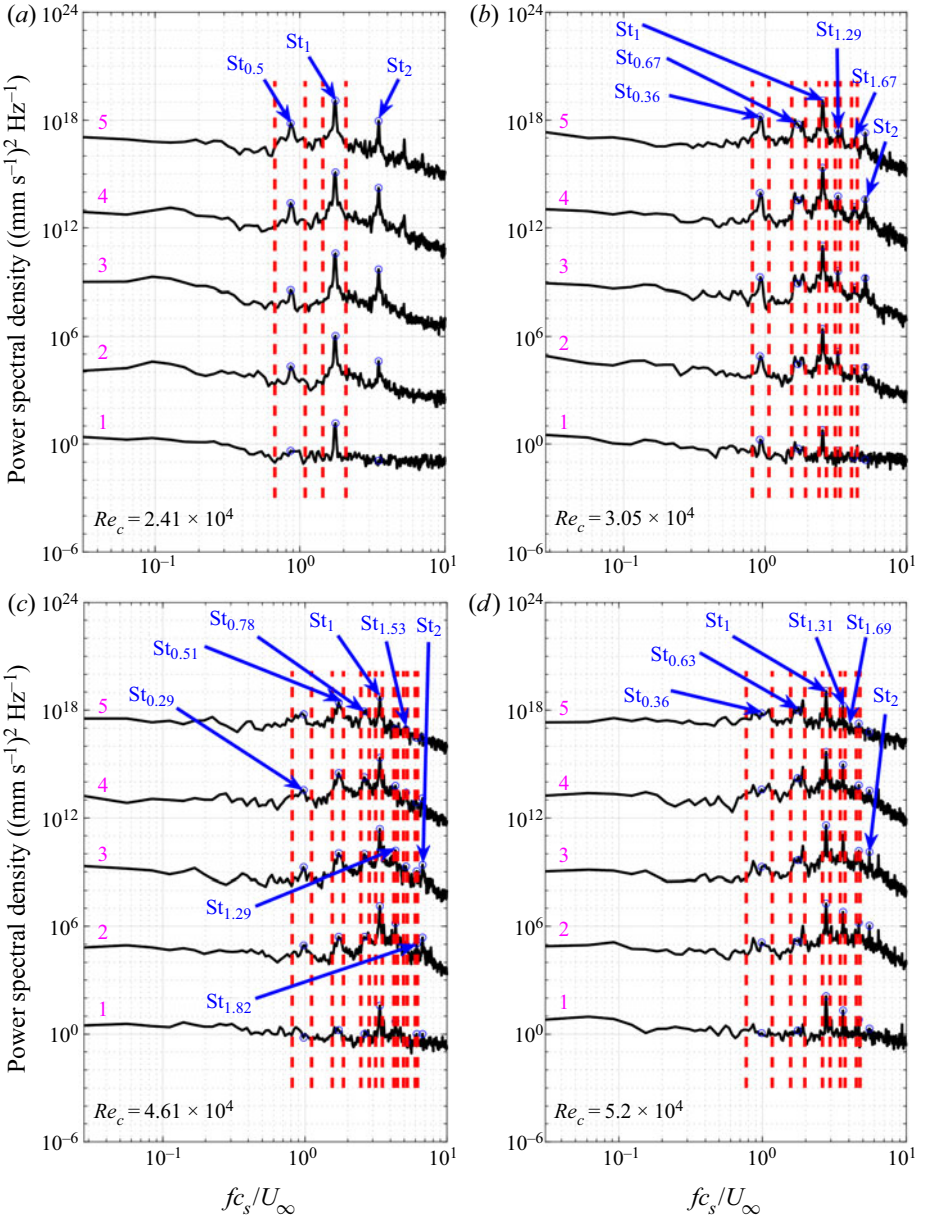

Figure 8. Power spectral densities in the slat cusp shear layer: (*a*) $Re_c = 2.41 \times 10^4$; (*b*) $Re_c = 3.05 \times 10^4$; (*c*) $Re_c = 4.61 \times 10^4$; (*d*) $Re_c = 5.2 \times 10^4$. The local power spectral densities of 1–5 are calculated from the v^{tran} signals at the probes 1–5 in figure 3, respectively. St_1 and St_2 denote the fundamental frequency and second harmonic, respectively. $St_{0.*}$ and $St_{1.*}$ denote the subharmonics and fractional harmonics, respectively. The red dashed lines define the frequency bands related to specific typical frequencies. The power spectral densities of each subfigure are amplified step by step by 10^4 along the probe positions for clarity.

a Re_c-dependence to a certain extent. Therefore, the flow physics of these subharmonics and fractional harmonics will be discussed in this section for all the four typical Re_c. Accordingly, specific frequency bands are defined in figure 8 (marked by red dashed lines) to contain the fluctuations pertaining to these frequency peaks, further promoting the

Re_c	Frequency peaks	Frequency bands (fc_s/U_∞)
2.41×10^4	$St_{0.5}$	0.67–1.09
	St_1	1.44–2.07
3.05×10^4	$St_{0.36}$	0.81–1.07
	$St_{0.67}$	1.54–1.93
	St_1	2.41–2.72
	$St_{1.29}$	3.14–3.39
	$St_{1.67}$	4.09–4.48
4.61×10^4	$St_{0.29}$	0.81–1.11
	$St_{0.51}$	1.56–1.87
	$St_{0.78}$	2.48–2.84
	St_1	3.15–3.51
	$St_{1.29}$	4.23–4.48
	$St_{1.53}$	4.96–5.26
	$St_{1.82}$	5.99–6.21
5.2×10^4	$St_{0.36}$	0.77–1.17
	$St_{0.63}$	1.57–1.97
	St_1	2.62–2.96
	$St_{1.31}$	3.48–3.76
	$St_{1.69}$	4.50–4.78

Table 1. The quantitative intervals of the frequency bands defined in figure 8.

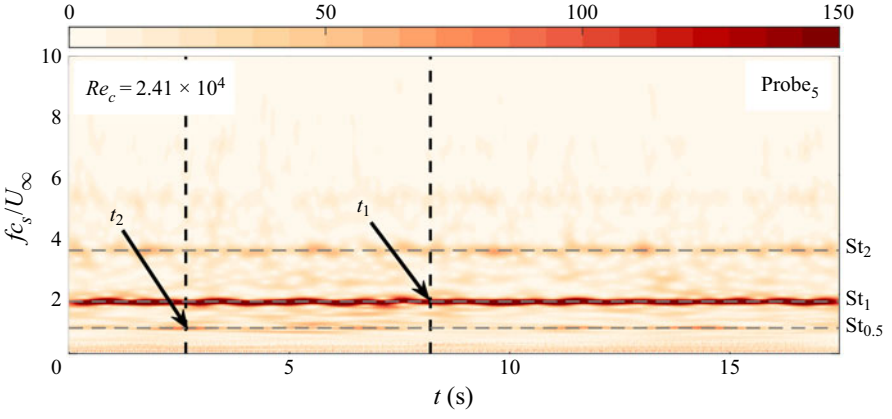

Figure 9. Wavelet spectrum of the v^{tran} signal at probe 5 (figure 3) of $Re_c = 2.41 \times 10^4$. Here, $St_{0.5}$, St_1 and St_2 denote the subharmonic, fundamental frequency and second harmonic, respectively; and t_1 and t_2 mark the absent and prominent instances of $St_{0.5}$, respectively.

physical analyses of subharmonics and fractional harmonics. The quantitative intervals of these frequency bands are provided in table 1.

4.3.1. *The $Re_c = 2.41 \times 10^4$ case*

The wavelet spectrum of the v^{tran} signal around the impingement locations is presented in figure 9. Similar to the cases of $1.38 \times 10^4 \leq Re_c \leq 1.83 \times 10^4$, St_1 persists and dominates the spectrum over the time interval. In contrast, the subharmonic $St_{0.5}$ appears intermittently over the time interval. When $St_{0.5}$ is absent in the spectrum

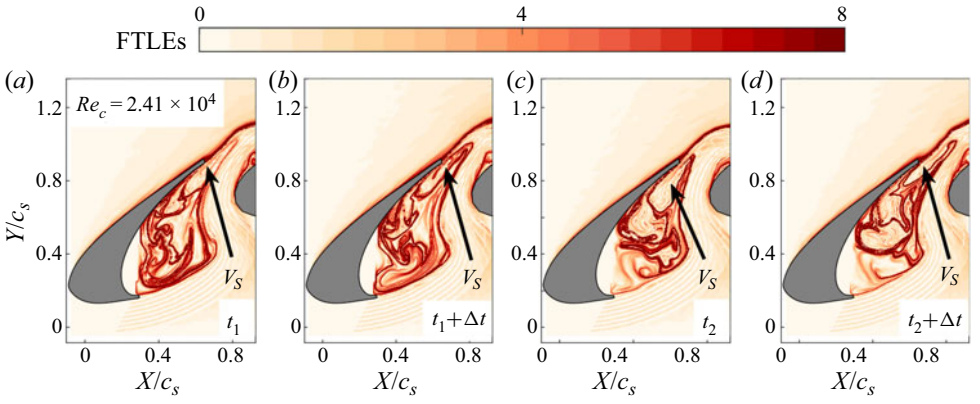

Figure 10. The LCSs revealed by the FTLEs method at $Re_c = 2.41 \times 10^4$. Here, V_S denotes the shed vortex of the free shear layer; t_1 and t_2 denote the absent and prominent instances of $\mathrm{St}_{0.5}$, respectively; and Δt is chosen as the shedding period of V_S.

(t_1 in figure 9), the impingement locations of two consecutive shed vortices are steady on the underside of the trailing edge (figure 10*a*,*b*), similar to the vortex dynamics of $1.38 \times 10^4 \leq Re_c \leq 1.83 \times 10^4$. When $\mathrm{St}_{0.5}$ is prominent in the spectrum (t_2 in figure 9), most parts of the shed vortices in the former and latter cycles are respectively entrained into the recirculation of the slat cove and pushed through the gap (figure 10*c*,*d*), which lead to unsteady impingement locations on the underside of the trailing edge. Therefore, the subharmonic $\mathrm{St}_{0.5}$ is related to the impingement of shed vortices with unsteady locations on the underside of the trailing edge.

To gain additional insight into the flow physics of $\mathrm{St}_{0.5}$, the reconstructed instantaneous fluctuations (v^{tran}) related to $\mathrm{St}_{0.5}$ and St_1 are shown in figures 11 and 12, respectively. When $\mathrm{St}_{0.5}$ is absent (t_1 in figure 9), the fluctuations related to $\mathrm{St}_{0.5}$ are weak in the slat cusp shear layer and the slat cove (figure 11*a–d*). When $\mathrm{St}_{0.5}$ is prominent (t_2 in figure 9), strong fluctuations related to $\mathrm{St}_{0.5}$ appear in the slat cusp shear layer (figure 11*e–h*). As indicated by the pattern in figure 11(*f*) (marked by a magenta ellipse), the impingement with unsteady locations can generate fluctuations of $\mathrm{St}_{0.5}$ and further disturb the slat cusp shear layer by the hydrodynamic feedback in the slat cove. Strong fluctuations of St_1 exist in the slat cusp shear layer regardless of whether $\mathrm{St}_{0.5}$ is prominent or not (figure 12), which is consistent with the vortex shedding patterns in figure 10. As unveiled by the pattern in figure 12(*b*) (marked by a magenta ellipse), the fluctuations originating from the impingement with the fundamental frequency can also disturb the slat cusp shear layer by the hydrodynamic feedback in the slat cove. In summary, the amplification of the subharmonic ($\mathrm{St}_{0.5}$) in the slat cusp shear layer leads to the shed vortices impinging on the underside of the trailing edge with unsteady impingement locations. The hydrodynamic feedback links the slat cusp and trailing edge.

4.3.2. *The $Re_c = 3.05 \times 10^4$ case*

As Re_c increases, more wavelet spectra at different probes are required to characterize the frequency properties of the slat cusp shear layer. Figure 13 shows the wavelet spectra extracted from the probes 5 and 3 in figure 3. The wavelet spectrum of probe 5 (figure 13*a*) is still employed to characterize the vortex dynamics around the impingement locations. According to the spectra in figure 8(*b*), the wavelet spectrum of probe 3 (figure 13*b*) is more suitable for characterizing the vortex dynamics at the early stage of the slat cusp

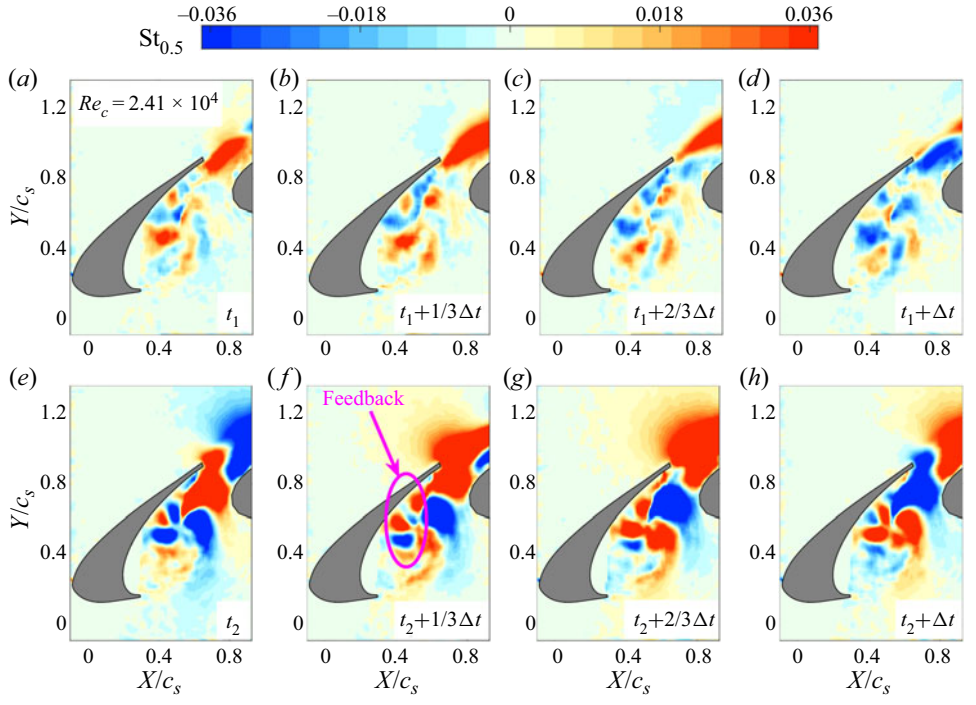

Figure 11. The reconstructed instantaneous velocity fields (normalized by U_∞) related to $\mathrm{St}_{0.5}$ at $Re_c = 2.41 \times 10^4$. Here, t_1 and t_2 denote the absent and prominent instances of $\mathrm{St}_{0.5}$, respectively; and Δt is chosen as the shedding period of V_S. Only the fluctuation components vertical to the main flow directions (v^{tran}) are contained in the fluctuation reconstruction.

shear layer. In figure 13(*b*), St_1 persists and dominates the spectrum over the time interval. The subharmonics ($\mathrm{St}_{0.36}$ and $\mathrm{St}_{0.67}$) and fractional harmonics ($\mathrm{St}_{1.29}$ and $\mathrm{St}_{1.67}$) have already appeared in the slat cusp shear layer intermittently. Around the impingement locations, $\mathrm{St}_{0.36}$ and $\mathrm{St}_{0.67}$ are intensified markedly and couple with each other (figure 13*a*). The vortex shedding pattern of St_1 is illustrated in figure 14(*a*) by the LCSs at t_1 of figure 13(*a*), when St_1 is the only prominent frequency. It is found that two consecutive shed vortices of the slat cusp shear layer (V_S^1 and V_S^2 in figure 14(*a*)) exist in the gap flow. When $\mathrm{St}_{0.36}$ and $\mathrm{St}_{0.67}$ are prominent (t_2 of figure 13(*a*)), there are still two consecutive shed vortices existing in the gap flow (V_S^1 and V_S^2 in figure 14(*b–d*)). The impingement locations of three consecutive shed vortices become unsteady: more of the first shed vortex is entrained into the recirculation of the slat cove (V_S^1 in figure 14(*b*)); more of the latter two shed vortices are pushed through the gap (V_S^1 in figure 14(*c*,*d*)). The instances of prominent $\mathrm{St}_{1.29}$ (t_3 of figure 13(*b*)) and $\mathrm{St}_{1.67}$ (t_4 of figure 13(*b*)) are found to contain three (V_S^1, V_S^2 and V_S^3 in figure 14(*e*)) and four (V_S^1, V_S^2, V_S^3 and V_S^4 in figure 14(*f*)) consecutive shed vortices in the gap flow, respectively. Therefore, the subharmonics are related to the impingement of shed vortices with unsteady locations on the underside of the trailing edge. The vortex shedding patterns related to the fractional harmonics contain more shed vortices in the gap flow than that of the fundamental frequency.

The reconstructed instantaneous fluctuations (v^{tran}) related to different specific frequencies (St_1, $\mathrm{St}_{0.36}$, $\mathrm{St}_{0.67}$, $\mathrm{St}_{1.29}$ and $\mathrm{St}_{1.67}$) are provided in figures 15–19. Figure 15 demonstrates that strong fluctuations pertaining to St_1 exist in the slat cusp shear layer regardless of whether the subharmonics and fractional harmonics are prominent or not.

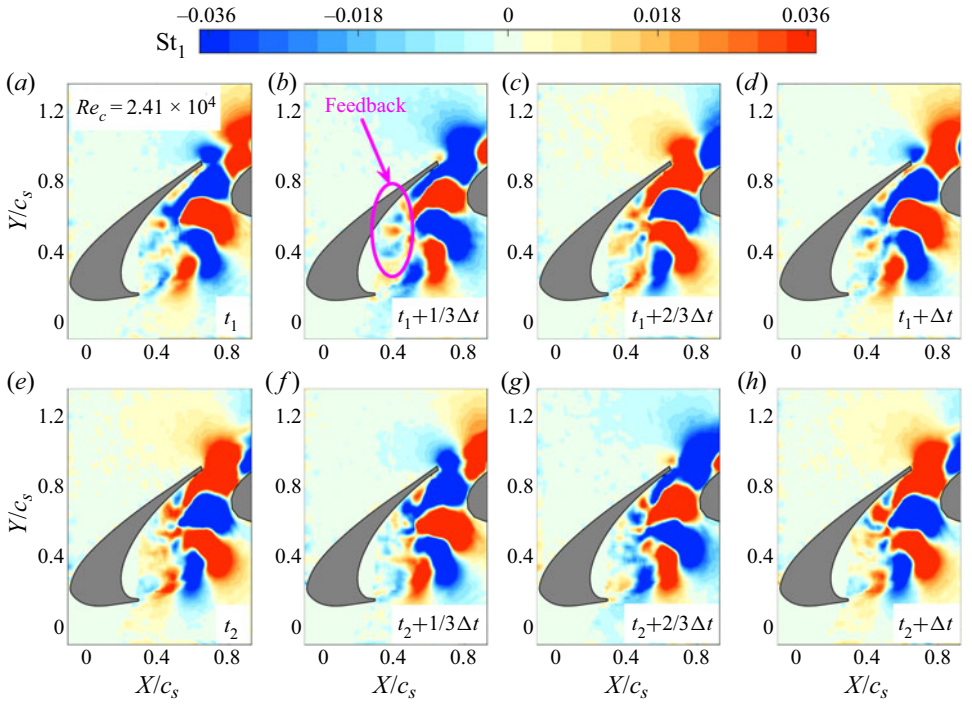

Figure 12. The reconstructed instantaneous velocity fields (normalized by U_∞) related to St_1 at $Re_c = 2.41 \times 10^4$. Here, t_1 and t_2 denote the absent and prominent instances of $\mathrm{St}_{0.5}$, respectively; and Δt is chosen as the shedding period of V_S. Only the fluctuation components vertical to the main flow directions (v^{tran}) are contained in the fluctuation reconstruction.

If the fully developed patterns with negative fluctuating velocities in figure 15 (marked by black ellipses) could be related to the discrete vortices identified in figure 14, two and only two vortices should exist in the gap flow of figure 14. However, this is not the case. Three and four discrete vortices exist in the gap flow of figures 14(*e*) and 14(*f*), respectively. Notably, the patterns of V_S^1 and V_S^2 in figure 14(*e*) and of V_S^1 and V_S^3 in figure 14(*f*) are comparable with those of V_S^1 and V_S^2 in figure 14(*a*). Therefore, the strong fluctuations in the slat cusp shear layer of figure 15(*e*) are attributed to the V_S^1 and V_S^2 in figure 14(*e*), while the strong fluctuations in the slat cusp shear layer of figure 15(*f*) are ascribed to the V_S^1 and V_S^3 in figure 14(*f*). Therefore, V_S^3 in figure 14(*e*) and V_S^2 and V_S^4 in figure 14(*f*) could be treated as the productions of the secondary instability in the braid region between two consecutive vortices (Smyth 2003). Additionally, the pattern in figure 15(*a*) (marked by a magenta ellipse) reveals the hydrodynamic feedback in the slat cove. The reconstructed instantaneous fluctuations pertaining to $\mathrm{St}_{0.36}$ and $\mathrm{St}_{0.67}$ are shown in figures 16 and 17, respectively. The unsteady impingement locations on the underside of the trailing edge (figure 14*b–d*) are found to correlate with the strong fluctuations related to $\mathrm{St}_{0.36}$ (figure 16*b–d*) and $\mathrm{St}_{0.67}$ (figure 17*b–d*) in the slat cusp shear layer. As shown in figure 13, the typical instance of $\mathrm{St}_{1.67}$ (t_4) also contains strong $\mathrm{St}_{0.36}$ and $\mathrm{St}_{0.67}$. Consequently, strong fluctuations related to $\mathrm{St}_{0.36}$ and $\mathrm{St}_{0.67}$ also appear in the slat cusp shear layer at t_4 (figures 16*f* and 17*f*). These strong fluctuations could make the shed vortices in figure 14(*f*) have unsteady impingement locations on the underside of the trailing edge. Again, the patterns in figures 16(*b–d*) and 17(*b–d*) (marked by magenta ellipses)

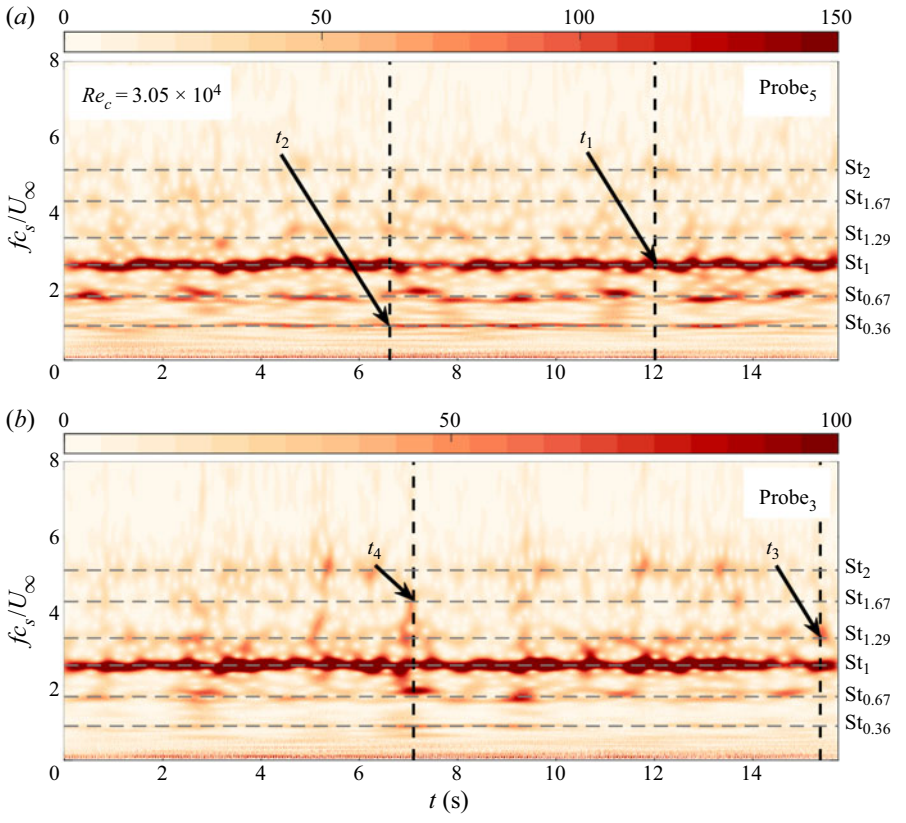

Figure 13. Wavelet spectra of the v^{tran} signals at different probes of $Re_c = 3.05 \times 10^4$: (*a*) probe 5 of figure 3; (*b*) probe 3 of figure 3. Here, St_1 and St_2 denote the fundamental frequency and second harmonic, respectively. Here, $St_{0.36}$ and $St_{0.67}$ denote the subharmonics; $St_{1.29}$ and $St_{1.67}$ denote the fractional harmonics; t_1, t_3 and t_4 mark the typical instances of St_1, $St_{1.29}$ and $St_{1.67}$, respectively; and t_2 marks the typical instant of $St_{0.36}$ and $St_{0.67}$.

demonstrate that the impingement with unsteady locations can generate fluctuations of subharmonics and further disturb the slat cusp shear layer by the hydrodynamic feedback in the slat cove. The vortex shedding patterns in figures 14(*e*) and 14(*f*) are respectively attributed to the strong fluctuations pertaining to $St_{1.29}$ (figure 18) and $St_{1.67}$ (figure 19) in the slat cusp shear layer. Because the pattern of V_S^1, V_S^3 and V_S^4 in figure 14(*f*) is comparable to that of V_S^1, V_S^2 and V_S^3 in figure 14(*e*), strong fluctuations related to $St_{1.29}$ also appear in the slat cusp shear layer of figure 18(*f*). In summary, the amplification of the subharmonics ($St_{0.36}$ and $St_{0.67}$) in the slat cusp shear layer leads to the unsteady impingement locations when the shed vortices impinge on the underside of the trailing edge. The fractional harmonics ($St_{1.29}$ and $St_{1.67}$) could trigger the secondary instability of the braid region between two consecutive vortices, which generates more shed vortices in the gap flow. The hydrodynamic feedback still links the slat cusp and trailing edge.

4.3.3. *The $Re_c = 4.61 \times 10^4$ case*

Following the methodology of figure 13, the wavelet spectra extracted from the probes 5 and 2 in figure 3 are provided in figure 20. St_1 still persists and dominates the spectrum over the time interval in figure 20(*b*). Additionally, the subharmonics ($St_{0.29}$,

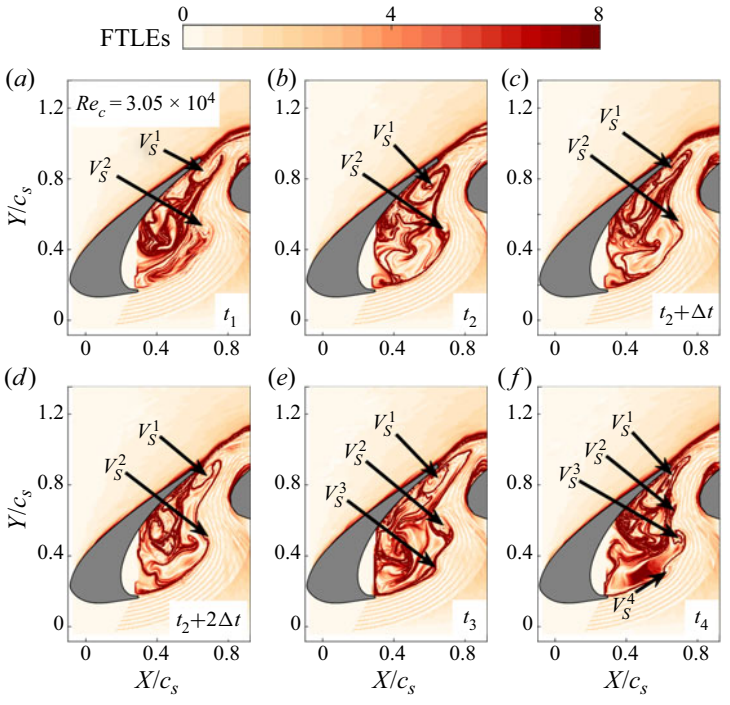

Figure 14. The LCSs revealed by the FTLEs method at $Re_c = 3.05 \times 10^4$: (*a*) at instant t_1 of figure 13; (*b–d*) at instant t_2 of figure 13; (*e*) at instant t_3 of figure 13; (*f*) at instant t_4 of figure 13. Here, V_S^1, V_S^2, V_S^3 and V_S^4 denote the shed vortices of the free shear layer; and Δt is chosen as the period of shed vortex with fundamental frequency.

$St_{0.51}$ and $St_{0.78}$) and fractional harmonics ($St_{1.29}$, $St_{1.53}$ and $St_{1.82}$) intermittently appear in figure 20(*b*). Similar to the case of $Re_c = 3.05 \times 10^4$, the subharmonics are markedly intensified around the impingement locations (figure 20*a*). The LCSs in figure 21(*a*) demonstrate the vortex shedding pattern of St_1 (t_1 of figure 20(*a*)). It is found that three shed vortices coexist in the gap flow (V_S^1, V_S^2 and V_S^3 in figure 21(*a*)). Similar to the case of $Re_c = 3.05 \times 10^4$, $St_{0.29}$ and $St_{0.78}$ correlate with the impingement of shed vortices with unsteady impingement locations: more of the first shed vortex is entrained into the recirculation of slat cove (V_S^1 in figure 21(*b*)); more of the latter two shed vortices are pushed through the gap (V_S^1 in figure 21(*c*,*d*)). For the typical instance of $St_{0.51}$ (t_3 of figure 20(*a*)), the shed vortices of the slat cusp shear layer still impinge on the underside of the trailing edge with unsteady impingement locations (figure 21*e–h*). The unsteady behaviour of the impingement locations in figure 21(*e–h*) is comparable to that pertaining to $St_{0.5}$ at $Re_c = 2.41 \times 10^4$ (figure 10*c*,*d*). When $St_{1.29}$ is prominent (t_4 of figure 20(*b*)), four shed vortices coexist in the gap flow (V_S^1, V_S^2, V_S^3 and V_S^4 in figure 21(*i*)). As expected, the gap flow contains five shed vortices (V_S^1, V_S^2, V_S^3, V_S^4 and V_S^5 in figure 21(*j*)) when $St_{1.82}$ is prominent (t_5 of figure 20(*b*)). Compared with those at $Re_c = 2.41 \times 10^4$ and $Re_c = 3.05 \times 10^4$, the instantaneous fluctuation reconstructions at $Re_c = 4.61 \times 10^4$ reveal similar flow physics and will not be shown for conciseness.

In summary, the amplification of subharmonics ($St_{0.29}$, $St_{0.51}$ and $St_{0.78}$) in the slat cusp shear layer leads to the unsteady impingement locations when the shed vortices impinge on the underside of the trailing edge. By triggering the secondary instability of the braid

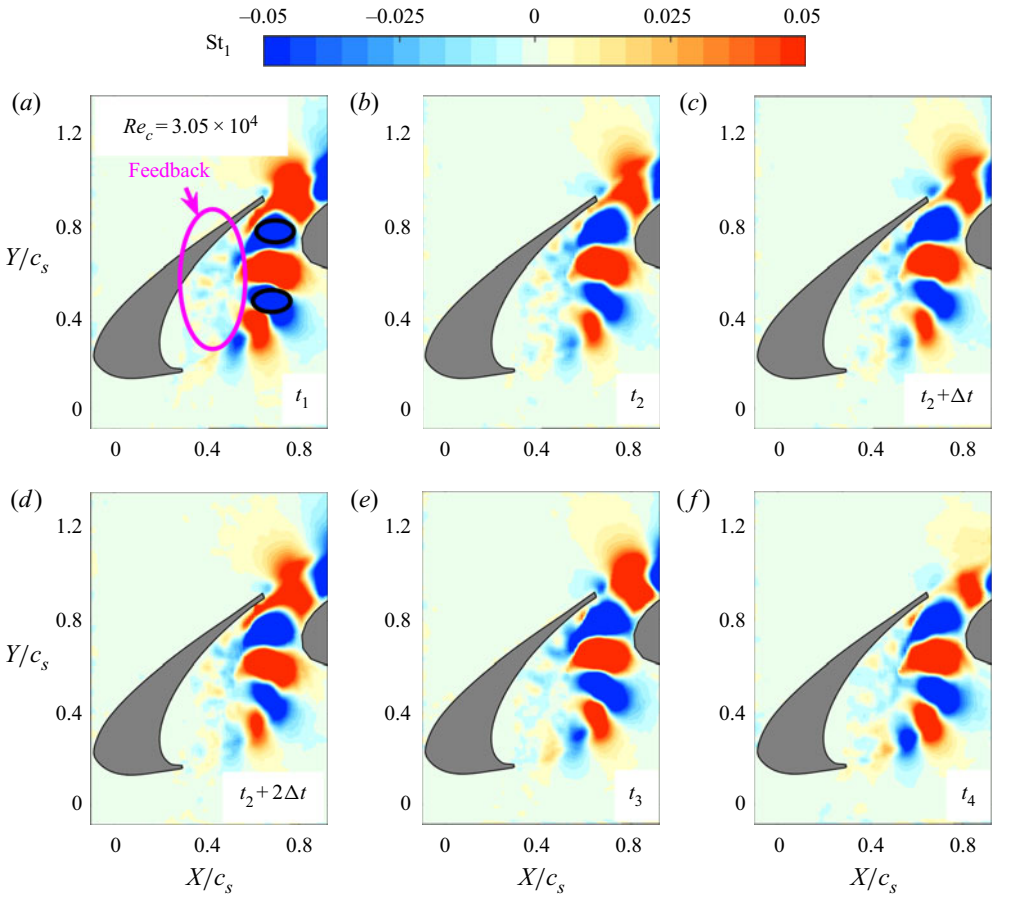

Figure 15. The reconstructed instantaneous velocity fields (normalized by U_∞) related to St_1 at $Re_c = 3.05 \times 10^4$: (*a*) at instant t_1 of figure 13; (*b–d*) at instant t_2 of figure 13; (*e*) at instant t_3 of figure 13; (*f*) at instant t_4 of figure 13. Here, Δt is chosen as the period of shed vortex with fundamental frequency. Only the fluctuation components vertical to the main flow directions (v^{tran}) are contained in the fluctuation reconstruction.

region, the fractional harmonics ($St_{1.29}$ and $St_{1.82}$) in the slat cusp shear layer could generate more shed vortices in the gap flow. The hydrodynamic feedback still links the slat cusp and trailing edge. It should be mentioned that the fractional harmonic of $St_{1.53}$ is too weak to trigger the secondary instability of the braid region. Therefore, no specific vortex shedding pattern related to $St_{1.53}$ is captured in the current work.

4.3.4. *The $Re_c = 5.2 \times 10^4$ case*

The wavelet spectra at probes 5 and 2 are presented in figure 22. At the early stage of the slat cusp shear layer, the dominant frequency switches between the fundamental frequency St_1 and the fractional harmonic $St_{1.31}$ (figure 22*b*), similar to the mode switching of the narrowband peaks at $Re_c \sim 10^6$ (Li *et al.* 2018*a*). Except for the time interval of 0.5–1.5 s, the left time interval in figure 22(*b*) is still dominated by St_1. In addition, the subharmonics ($St_{0.36}$ and $St_{0.63}$) and another fractional harmonic ($St_{1.69}$) intermittently appear in the slat cusp shear layer at the early stage (figure 22*b*). Similar to the cases of

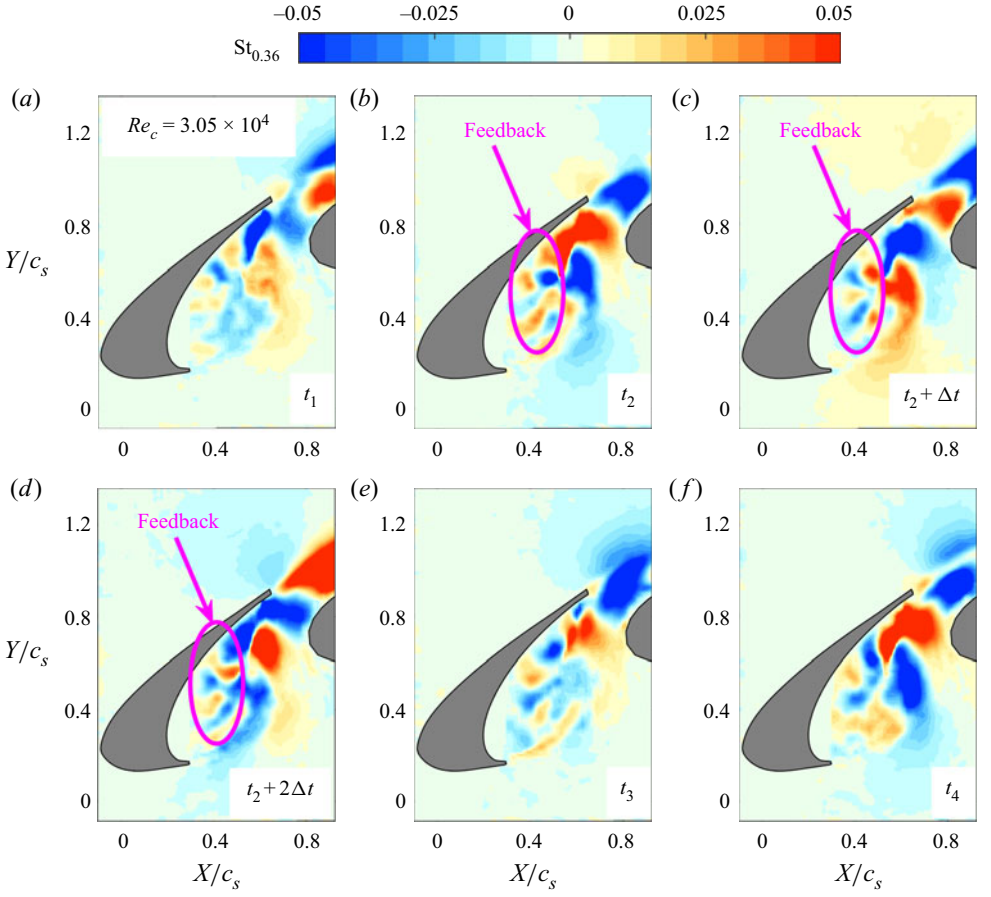

Figure 16. The reconstructed instantaneous velocity fields (normalized by U_∞) related to $St_{0.36}$ at $Re_c = 3.05 \times 10^4$: (*a*) at instant t_1 of figure 13; (*b–d*) at instant t_2 of figure 13; (*e*) at instant t_3 of figure 13; (*f*) at instant t_4 of figure 13. Here, Δt is chosen as the period of shed vortex with fundamental frequency. Only the fluctuation components vertical to the main flow directions (v^{tran}) are contained in the fluctuation reconstruction.

$Re_c = 3.05 \times 10^4$ and $Re_c = 4.61 \times 10^4$, the subharmonics are markedly intensified around the impingement locations (figure 22*a*). The LCSs in figure 23(*a*) show that three shed vortices (V_S^1, V_S^2 and V_S^3) coexist in the gap flow at the typical instance of St_1 (t_1 in figure 22(*a*)). The subharmonics are found to correlate with the impingement of shed vortices with unsteady impingement locations (figure 23*b–d*), similar to the scenarios of $Re_c = 2.41 \times 10^4$, $Re_c = 3.05 \times 10^4$ and $Re_c = 4.61 \times 10^4$. For the typical instance of $St_{1.31}$ (t_3 in figure 22(*b*)), the gap flow simultaneously contains four shed vortices (V_S^1, V_S^2, V_S^3 and V_S^4 in figure 23(*e*)). While for the typical instance of $St_{1.69}$ (t_4 in figure 22(*b*)), there are five shed vortices (V_S^1, V_S^2, V_S^3, V_S^4 and V_S^5 in figure 23(*f*)) in the gap flow. The instantaneous fluctuation reconstructions are still employed to add more insights into the specific frequencies mentioned above. The resulted conclusions at $Re_c = 5.2 \times 10^4$ are strongly similar to those at $Re_c = 2.41 \times 10^4$, $Re_c = 3.05 \times 10^4$ and $Re_c = 4.61 \times 10^4$. As a result, the reconstructed instantaneous fluctuations are not provided here for conciseness.

In summary, the strong fluctuations of $St_{0.36}$ and $St_{0.63}$ in the slat cusp shear layer make the shed vortices have unsteady impingement locations on the underside of the

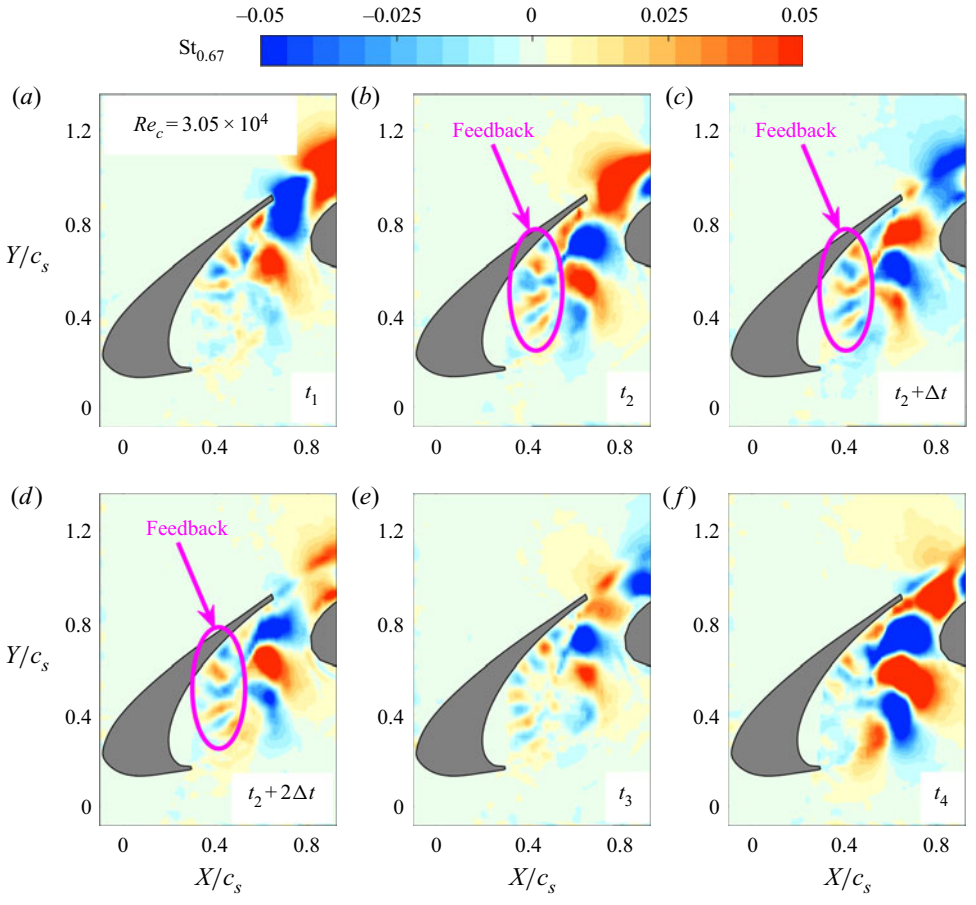

Figure 17. The reconstructed instantaneous velocity fields (normalized by U_∞) related to $St_{0.67}$ at $Re_c = 3.05 \times 10^4$: (*a*) at instant t_1 of figure 13; (*b–d*) at instant t_2 of figure 13; (*e*) at instant t_3 of figure 13; (*f*) at instant t_4 of figure 13. Here, Δt is chosen as the period of shed vortex with fundamental frequency. Only the fluctuation components vertical to the main flow directions (v^{tran}) are contained in the fluctuation reconstruction.

trailing edge. $St_{1.31}$ and $St_{1.69}$ in the slat cusp shear layer contribute to more shed vortices in the gap flow by triggering the secondary instability of the braid region. The mode switching in the spectra of the slat flow is attributed to the switching between different vortex shedding patterns of the slat cusp shear layer. The hydrodynamic feedback links the slat cusp and trailing edge.

5. Extending the vortex dynamics to high Reynolds numbers

The links of slat flows between low and high Reynolds numbers will be discussed in this section. As reported by Murayama *et al.* (2014), Pascioni & Cattafesta (2016) and Li *et al.* (2018*b*), the dimensional frequencies of the narrowband peaks at $Re_c \sim 10^6$ are approximately 10^3 Hz, which are higher than those in the current work ($\sim 10^1$ Hz). However, the non-dimensional Strouhal numbers of these narrowband peaks in the current work (approximately 1–5 in figure 8) are comparable to those at $Re_c \sim 10^6$, which strongly indicates the potential relations between the slat flows at $Re_c \sim 10^4$ and

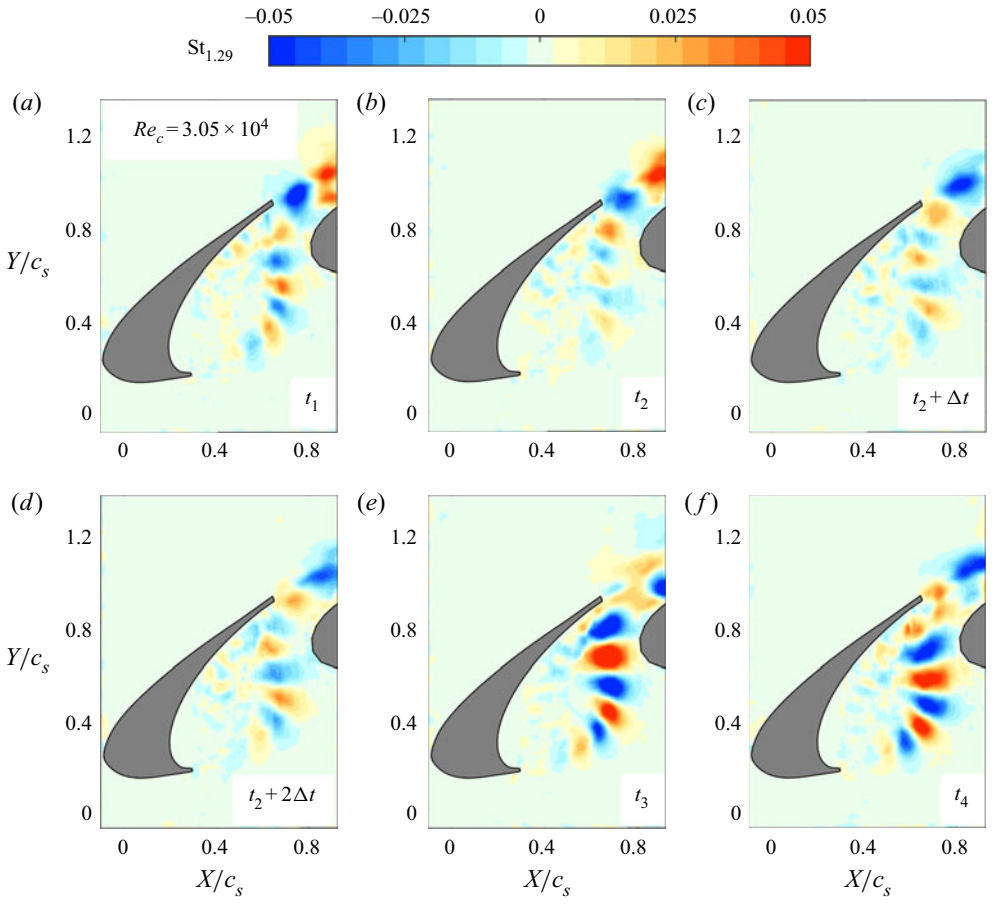

Figure 18. The reconstructed instantaneous velocity fields (normalized by U_∞) related to $St_{1.29}$ at $Re_c = 3.05 \times 10^4$: (*a*) at instant t_1 of figure 13; (*b–d*) at instant t_2 of figure 13; (*e*) at instant t_3 of figure 13; (*f*) at instant t_4 of figure 13. Here, Δt is chosen as the period of shed vortex with fundamental frequency. Only the fluctuation components vertical to the main flow directions (v^{tran}) are contained in the fluctuation reconstruction.

$Re_c \sim 10^6$. The discussions in this section indicate that the vortex dynamics in the range of $2.41 \times 10^4 \leq Re_c \leq 5.2 \times 10^4$ could persist to the range of $Re_c \sim 10^6$.

The ratios of other typical frequencies to the fundamental frequency are presented in figure 24. All benchmark databases at $Re_c \sim 10^6$ of figure 24 show the investigations at the geometric angles of attack comparable to the current work. Notably, the slight deviations of geometric angle of attack between the benchmark databases and the current work do not affect the flow physics revealed by figure 24, because narrowband peaks robustly exist in the spectra with different angles of attack to a certain extent (Kolb *et al.* 2007; Imamura *et al.* 2009; Murayama *et al.* 2014; Herr *et al.* 2015; Pagani, Souza & Medeiros 2016, 2017). Surprisingly, the subharmonics and fractional harmonics observed in the range of $2.41 \times 10^4 \leq Re_c \leq 5.2 \times 10^4$ still exist in the slat flow at $Re_c \sim 10^6$. Moreover, the ratios of subharmonics to the fundamental frequency are located around $1/3St_1$, $1/2St_1$ and $2/3St_1$, while the ratios of fractional harmonics to the fundamental frequency are located around $4/3St_1$, $3/2St_1$ and $5/3St_1$. This universal law indicates that the vortex dynamics in the current low-Reynolds-number range ($2.41 \times 10^4 \leq Re_c \leq 5.2 \times 10^4$) could persist to the

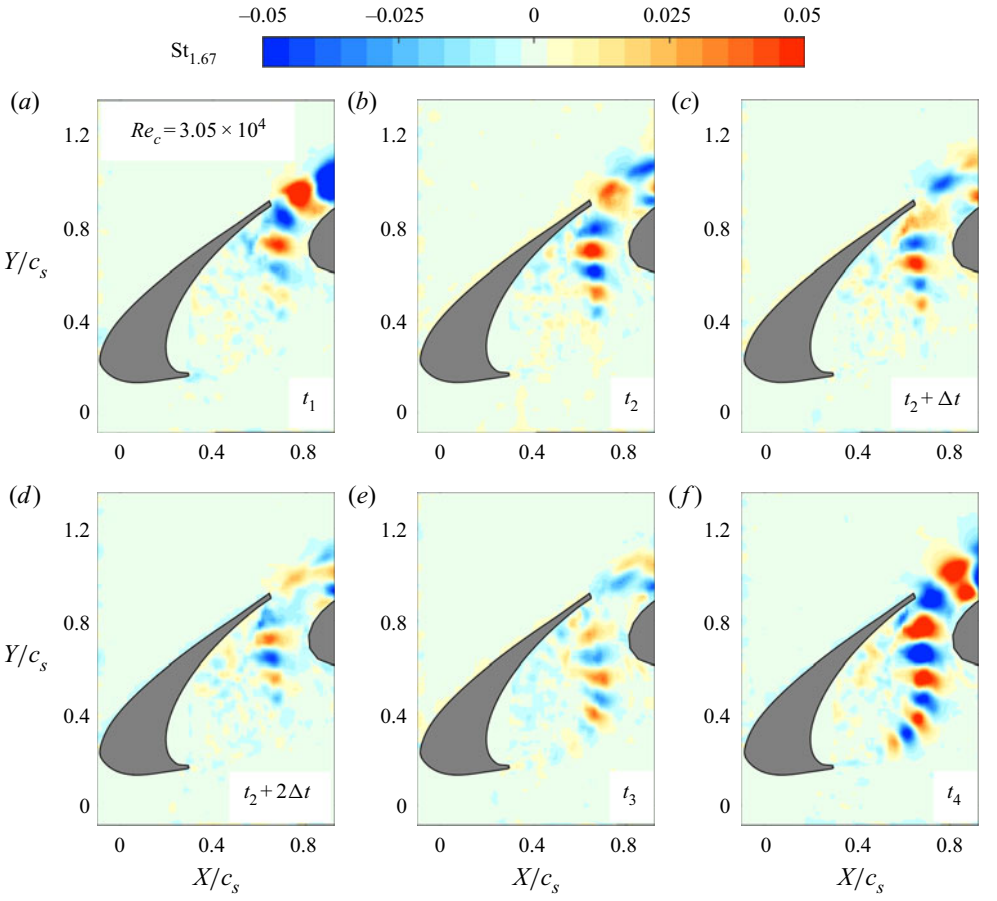

Figure 19. The reconstructed instantaneous velocity fields (normalized by U_∞) related to $\mathrm{St}_{1.67}$ at $Re_c = 3.05 \times 10^4$: (*a*) at instant t_1 of figure 13; (*b–d*) at instant t_2 of figure 13; (*e*) at instant t_3 of figure 13; (*f*) at instant t_4 of figure 13. Here, Δt is chosen as the period of shed vortex with fundamental frequency. Only the fluctuation components vertical to the main flow directions (v^{tran}) are contained in the fluctuation reconstruction.

high-Reynolds-number range ($Re_c \sim 10^6$). This conjecture can be further verified by the massive similarities of the vortex dynamics between low and high Reynolds numbers:

(i) In the range of $2.41 \times 10^4 \leq Re_c \leq 5.2 \times 10^4$, the shed vortices of the slat cusp shear layer can impinge on the underside of the trailing edge with unsteady impingement locations, similar to the scenario where the shed vortices could be either entrained into the recirculation of slat cove or pushed through the gap at $Re_c \sim 10^6$ (Jenkins *et al*. 2004; Deck & Laraufie 2013).

(ii) When $Re_c \geq 4.61 \times 10^4$, the single-recirculation pattern in the slat cove is comparable with the topology of the slat cove at $Re_c \sim 10^6$ (Jenkins *et al*. 2004; Pascioni *et al*. 2014). As mentioned in § 3, the slat cusp shear layer reattaches on the underside of the trailing edge. The distance between the trailing edge and the reattachment location is estimated to be $0.1c_s$ at $Re_c = 5.2 \times 10^4$, which is consistent with the estimation of Jenkins *et al*. (2004) at $Re_c = 3.64 \times 10^6$.

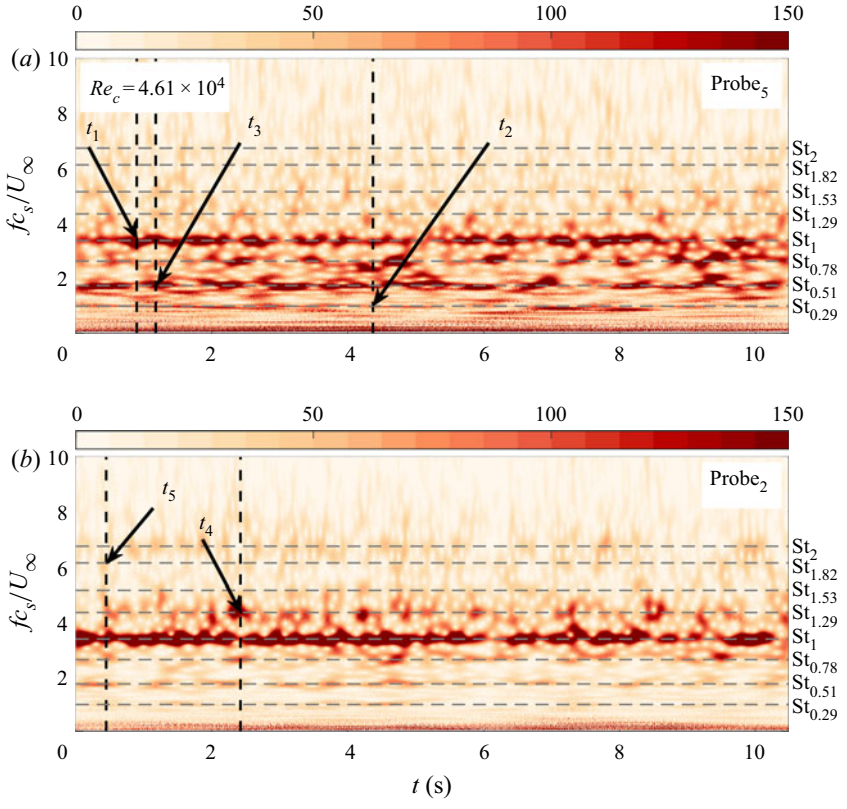

Figure 20. Wavelet spectra of the v^{tran} signals at different probes of $Re_c = 4.61 \times 10^4$: (*a*) probe 5 of figure 3; (*b*) probe 2 of figure 3. Here, St_1 and St_2 denote the fundamental frequency and second harmonic, respectively; $St_{0.29}$, $St_{0.51}$ and $St_{0.78}$ denote the subharmonics; $St_{1.29}$, $St_{1.53}$ and $St_{1.82}$ denote the fractional harmonics; t_1, t_4 and t_5 mark the typical instances of St_1, $St_{1.29}$ and $St_{1.82}$, respectively; t_2 marks the typical instant of $St_{0.29}$ and $St_{0.78}$; and t_3 marks the typical instant of $St_{0.51}$.

(iii) As visualized by the λ_2 criterion, four large-scale shed vortices coexist in the gap flow of Souza *et al.* (2019) ($Re_c = 1 \times 10^6$). The gap flow at $Re_c = 5.2 \times 10^4$ can also contain four large-scale shed vortices according to the LCSs extracted by the FTLEs method.

(iv) Li *et al.* (2018*a*) observed the mode switching of the narrowband peaks in the far-field noise spectrum at $Re_c \sim 10^6$. It is found that mode switching also occurs to the vortex shedding patterns of the slat cusp shear layer at $Re_c = 5.2 \times 10^4$.

Notably, Pascioni & Cattafesta (2018*a*,*b*) reported that a low frequency peak existed in the surface pressure spectra near the reattachment point of the slat cusp shear layer at $Re_c \sim 10^6$. The frequency of this special peak was one order of magnitude lower than the fundamental frequency (St_1), which led to the related Strouhal number of approximately $0.1St_1$. The phase-averaged results of Pascioni & Cattafesta (2018*b*) indicated that the fundamental frequency was related to the shed vortices of the slat cusp shear layer. The modal analyses by Pascioni & Cattafesta (2018*b*) revealed that the low frequency peak ($0.1St_1$) was attributed to the flapping, rather than the shed vortices, of the slat cusp shear layer. In contrast, figures 11, 16 and 17 indicate that the subharmonics are related to the shed vortices of the slat cusp shear layer. Therefore, the flow physics of the low frequency

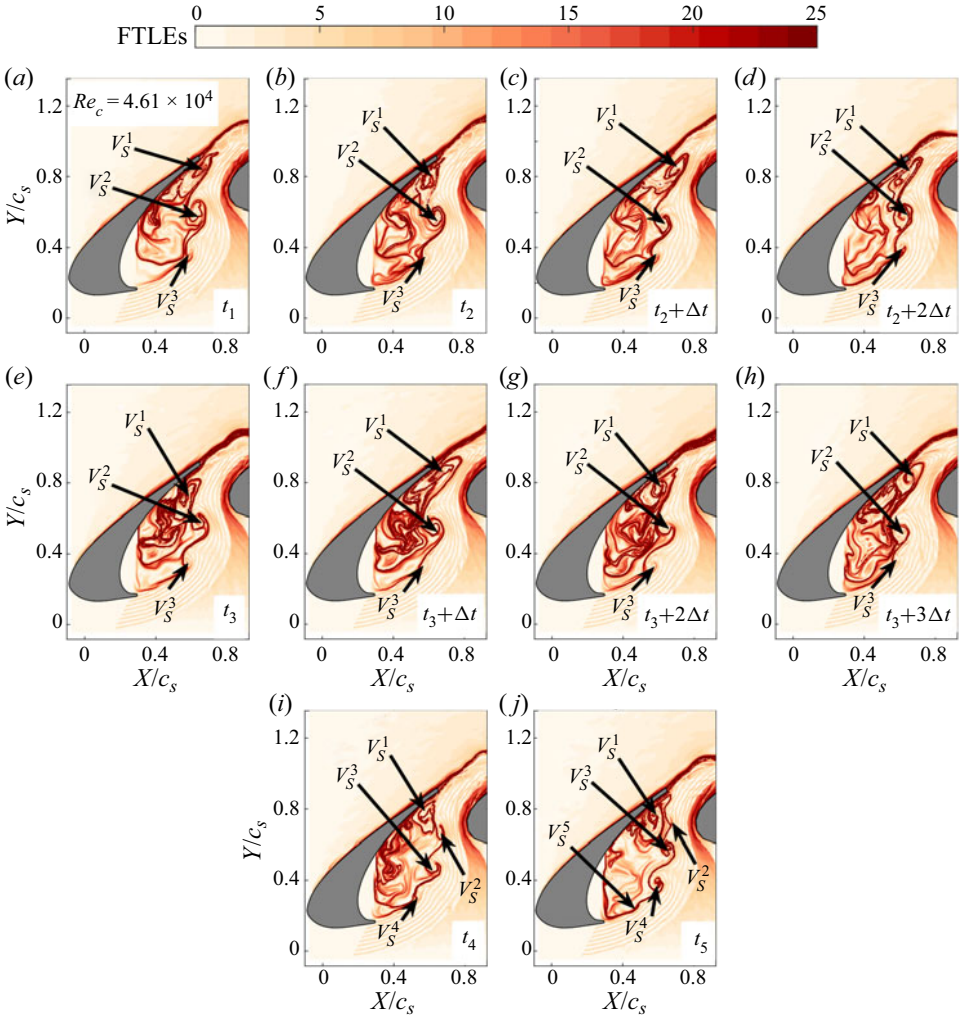

Figure 21. The LCSs revealed by the FTLEs method at $Re_c = 4.61 \times 10^4$: (*a*) at instant t_1 of figure 20; (*b–d*) at instant t_2 of figure 20; (*e–h*) at instant t_3 of figure 20; (*e*) at instant t_4 of figure 20; (*f*) at instant t_5 of figure 20. Here, V_S^1, V_S^2, V_S^3, V_S^4 and V_S^5 denote the shed vortices of the free shear layer; and Δt is chosen as the period of shed vortex with fundamental frequency.

peak ($0.1\mathrm{St}_1$) reported by Pascioni & Cattafesta (2018*a*,*b*) is different from that of the subharmonics in the current work, although these two kinds of frequency peaks can lead to similarly unsteady reattachment (or impingement) of the slat cusp shear layer on the underside of the slat trailing edge. Unfortunately, the low frequency peak ($0.1\mathrm{St}_1$) reported by Pascioni & Cattafesta (2018*a*,*b*) is too low to be captured in the current measurements, because the recording time of PIV is limited by the onboard memory of the camera. As a result, the effects of shear layer flapping on the vortex dynamics of slat flows cannot be discussed in the current work.

According to Terracol *et al*. (2015) and Souza *et al*. (2019), the narrowband peaks at $Re_c \sim 10^6$ should be attributed to the aeroacoustic feedback in the slat cove. The shed vortices of the slat cusp shear layer impinge on the underside of the trailing edge and generate fluctuations around the impingement locations. These fluctuations are convected

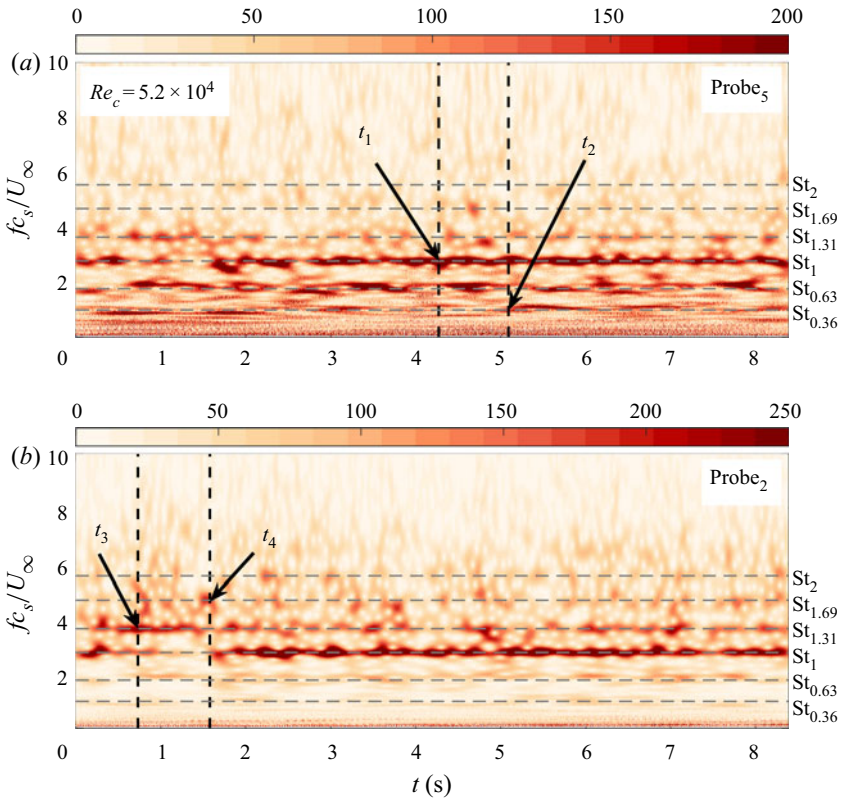

Figure 22. Wavelet spectra of the v^{tran} signals at different probes of $Re_c = 5.2 \times 10^4$: (*a*) probe 5 of figure 3; (*b*) probe 2 of figure 3. Here, St_1 and St_2 denote the fundamental frequency and second harmonic, respectively; $St_{0.36}$ and $St_{0.63}$ denote the subharmonics; $St_{1.31}$ and $St_{1.69}$ denote the fractional harmonics; t_1, t_3 and t_4 mark the typical instances of St_1, $St_{1.31}$ and $St_{1.69}$, respectively; and t_2 marks the typical instant of $St_{0.36}$ and $St_{0.63}$.

to the slat cusp with the speed of sound. Consequently, the aeroacoustic feedback links the slat cusp and trailing edge. While for the current low-Reynolds-number case, the fluctuations, which originate from the impingement of shed vortices on the underside of the trailing edge, are convected to the slat cusp with the speed of the recirculation in the slat cove. As a result, a hydrodynamic feedback links the slat cusp and trailing edge. It seems like different kinds of feedback lead to similar narrowband peaks. The relations between the aeroacoustic feedback and the hydrodynamic feedback are therefore discussed here to figure out this 'contradiction':

(i) The aeroacoustic feedback and the hydrodynamic feedback are intrinsically similar. The fluctuations for feedback in these two mechanisms both originate from the interactions between the shed vortices of the slat cusp shear layer and the underside surface of the slat trailing edge (Dobrzynski 2010; Deck & Laraufie 2013; Terracol *et al*. 2015; Pascioni & Cattafesta 2018*b*; Souza *et al*. 2019). The aeroacoustic feedback reported by Terracol *et al*. (2015) and Souza *et al*. (2019) could be generally treated as a kind of hydrodynamic feedback, if the traveling speed of fluctuations (sound speed) is replaced by the speed of the recirculation in the slat cove.

(ii) The different feedback speeds between the aeroacoustic feedback and the hydrodynamic feedback do not affect the non-dimensional Strouhal numbers of

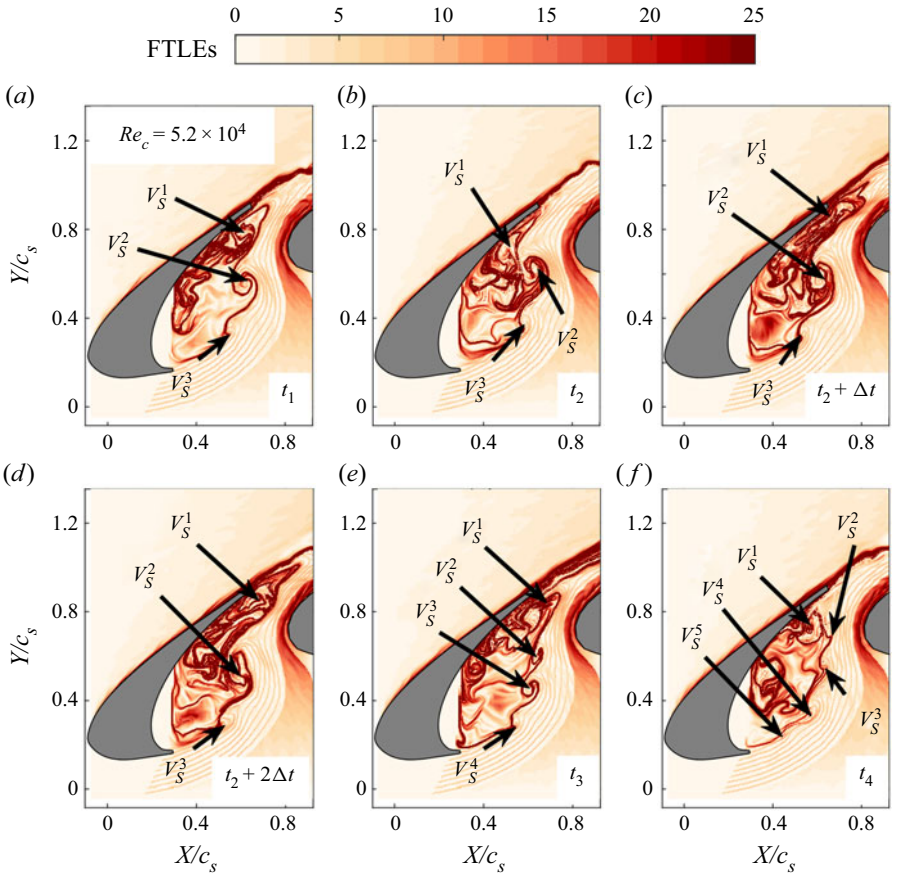

Figure 23. The LCSs revealed by the FTLEs method at $Re_c = 5.2 \times 10^4$: (*a*) at instant t_1 of figure 22; (*b–d*) at instant t_2 of figure 22; (*e*) at instant t_3 of figure 22; (*f*) at instant t_4 of figure 22. Here, V_S^1, V_S^2, V_S^3, V_S^4 and V_S^5 denote the shed vortices of the free shear layer; and Δt is chosen as the period of shed vortex with fundamental frequency.

narrowband peaks. The selection of narrowband peaks in the current hydrodynamic feedback is similar to that in the aeroacoustic feedback at $Re_c \sim 10^6$. The prediction equation for narrowband peaks (f_n) in the aeroacoustic feedback, improved by Terracol *et al*. (2015), is

$$f_n = (n_a + n_v)\frac{U_v(c_0 - U_a)}{L_a U_v + L_v(c_0 - U_a)}, \tag{5.1}$$

where U_v is the convection velocity of the fluctuations in the slat cusp shear layer, c_0 is the speed of sound, U_a is the mean velocity component inside the slat cove and is opposite to the convection direction of returning acoustic fluctuations, L_v and L_a are respectively the shear layer length and the acoustic feedback path, n_a is the wavenumber of the returning acoustic fluctuations in the slat cove, n_v is the wavenumber of the fluctuations in the slat cusp shear layer. Compared with c_0, U_a has negligible effects on the acoustic feedback path and therefore can be neglected. The non-dimensional prediction equation (using the freestream velocity U_∞ and the

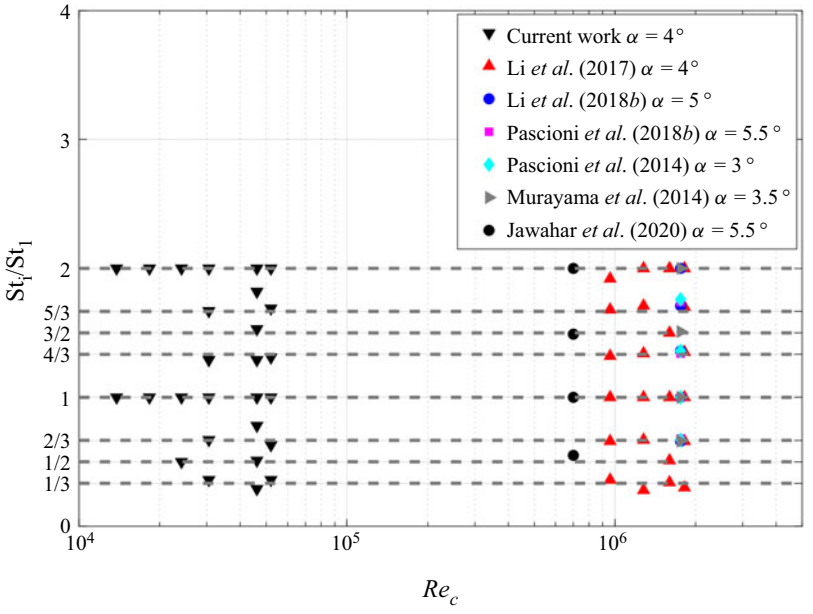

Figure 24. Ratios of other typical frequencies to the fundamental frequency.

slat chord length c_s) is then written as

$$\mathrm{St}_n = (n_a + n_v)\left(\frac{L_a}{c_s}\frac{U_\infty}{c_0} + \frac{L_v}{c_s}\frac{U_\infty}{U_v}\right)^{-1}. \tag{5.2}$$

The large feedback speed (c_0) can immediately convect the fluctuations around the slat trailing edge to the slat cusp, which leads to the term of U_∞/c_0 in (5.2) of around 0.1 (Terracol *et al.* 2015; Souza *et al.* 2019). As a result, the slat cusp shear layer can be disturbed by the fluctuations around the slat trailing edge in a rapid manner at $Re_c \sim 10^6$. The n_a in (5.2) therefore equals 1 for the aeroacoustic feedback, which is supported by figure 22 of Souza *et al.* (2019). Following the strategies of Terracol *et al.* (2015), the non-dimensional prediction equation for the current hydrodynamic feedback could be proposed as

$$\mathrm{St}_n = (n_h + n_v)\left(\frac{L_h}{c_s}\frac{U_\infty}{U_h} + \frac{L_v}{c_s}\frac{U_\infty}{U_v}\right)^{-1}. \tag{5.3}$$

The feedback speed of c_0, the acoustic feedback path L_a and the wavenumber of the returning acoustic fluctuations in the slat cove n_a in (5.2) are replaced by the speed of recirculation U_h, the hydrodynamic feedback path L_h and the wavenumber of the returning hydrodynamic fluctuations in the slat cove n_h in (5.3), respectively. Because of the small value of U_h, the term of U_∞/U_h in (5.3) is estimated to be approximately 5 for the current hydrodynamic feedback, which is larger than the term of U_∞/c_0 in (5.2). As a result, the fluctuations around the slat trailing edge need a longer time to be convected to the slat cusp at $Re_c \sim 10^4$. Therefore, there is a time delay for the fluctuations around the slat trailing edge to disturb the slat cusp shear layer at $Re_c \sim 10^4$. Notably, the fluctuations for hydrodynamic feedback originate from the interactions between the shed vortices of the slat cusp shear layer and the

underside surface of the slat trailing edge at $Re_c \sim 10^4$. Although the slat cusp shear layer cannot be immediately disturbed by the fluctuations generated in the current vortex shedding cycle, it can immediately be disturbed by the fluctuations generated in some former vortex shedding cycle. Because the periodic vortex shedding related to a specific narrowband peak can robustly persist for a period, the fluctuations with similar frequency properties fill the feedback path in the slat cove (figures 11–12 and 15–17). As a result, the slat cusp shear layer can immediately be disturbed by the fluctuations comparable to those generated in the current vortex shedding cycle. Therefore, the term of n_h in (5.3) is larger than 3 for the current hydrodynamic feedback (figures 11–12 and 15–17), which is larger than the n_a in (5.2). Except for the two terms of n_a and U_∞/c_0 in (5.2) and of n_h and U_∞/U_h in (5.3), the other terms in these two equations have comparable values (supported by the current results and the results reported by Terracol *et al*. (2015) and Souza *et al*. (2019)). As a result, the large n_h and U_∞/U_h in (5.3) still lead to a St_n around 1–5, comparable to that of (5.2). Therefore, the different feedback speeds do not change the intrinsic similarity between the aeroacoustic feedback and the hydrodynamic feedback. The coupled variations of the feedback fluctuation wavenumber (n_a in (5.2) and n_h in (5.3)) and the feedback speed (U_∞/c_0 in (5.2) and U_∞/U_h in (5.3)) result in similar non-dimensional Strouhal numbers between the aeroacoustic feedback and the current hydrodynamic feedback. Although the amplitudes of the returning hydrodynamic fluctuations in the slat cove could be sufficiently high to trigger the instability of the slat cusp shear layer, they are too low to accurately determine the n_h in (5.3). Therefore, (5.3) fails to accurately predict the narrowband peaks in figure 8. Reliable time-resolved databases of the slat flows, with higher accuracy to determine the n_h in (5.3), should be pursued in future work to improve (5.3).

(iii) The shed vortices of the slat cusp shear layer at $Re_c \sim 10^6$ (aeroacoustic feedback) should contain more turbulence than those at $Re_c \sim 10^4$ (hydrodynamic feedback). However, this difference does not affect the non-dimensional Strouhal numbers of the narrowband peaks. Souza *et al*. (2019) found that the large-scale shed vortices, rather than the small-scale turbulence, were relevant to the radiation of narrowband peaks. Because the vortex dynamics of $Re_c \sim 10^6$ and $Re_c \sim 10^4$ are found to be comparable with each other in large-scale flow structures, the narrowband peaks related to these two kinds of feedback should have similar non-dimensional Strouhal numbers.

(iv) The aeroacoustic feedback and the hydrodynamic feedback can coexist or couple with each other at $Re_c \sim 10^4$ and $Re_c \sim 10^6$. Although they cannot be captured in the current measurements, the pressure waves, generated by the impingement of shed vortices on the underside of trailing edge, are expected to be convected to the slat cusp with the speed of sound at $Re_c \sim 10^4$. This kind of process can therefore be depicted by (5.2). Owing to the large value of c_0 ($c_0 \approx 1500\ \mathrm{m\ s^{-1}} \gg U_\infty$), the term related to U_∞/c_0 can be neglected and n_a equals 0. As a result, (5.2) can be simplified and manipulated as

$$\mathrm{St}_n = n_v\left(\frac{L_v}{c_s}\frac{U_\infty}{U_v}\right)^{-1} = n_v\left(\frac{L_v}{U_v}\frac{U_\infty}{c_s}\right)^{-1} = n_v\left(t_v\frac{U_\infty}{c_s}\right)^{-1}, \tag{5.4}$$

where t_v is the convection time of disturbances inside the slat cusp shear layer from the slat cusp to the trailing edge and is directly calculated from the current time-resolved measurements. Similar to (5.3), (5.4) is also found to provide a

predicted St_n around 1–5, which indicates the potential effects of aeroacoustic feedback at $Re_c \sim 10^4$. However, many investigations have reported that the shed vortices of the slat cusp shear layer can be entrained into the recirculation in the slat cove and further convected to the slat cusp at $Re_c \sim 10^6$ (Jenkins *et al*. 2004; Choudhari & Khorrami 2007; Deck & Laraufie 2013), similar to the scenario of the current hydrodynamic feedback. It is therefore deduced that the hydrodynamic feedback discussed in the current work can persist to the range of $Re_c \sim 10^6$ and coexist with the aeroacoustic feedback. However, how these two kinds of feedback couple with each other still needs to be further investigated with time-resolved databases at $Re_c \sim 10^6$. Notably, Choudhari & Khorrami (2007) found that some recirculating structures can mainly trigger the three-dimensional instability of the shed vortices formed near the slat cusp, rather than trigger the vortex shedding of the slat cusp shear layer. However, this does not mean that all recirculating structures and acoustic waves inside the slat cove will destroy the shed vortices of the slat cusp shear layer and weaken/vanish the narrowband peaks. Some other recirculating structures and acoustic waves are conjectured to trigger the vortex shedding of the slat cusp shear layer and therefore contribute to the feedback in the slat cove. This conjecture is supported by Souza *et al*. (2019). Souza *et al*. (2019) found that two-dimensional large-scale shed vortices played an important role in the aeroacoustic feedback at $Re_c \sim 10^6$, although the slat cove flow was strongly three-dimensional. The current work also supports this conjecture. Notably, the current recirculation inside the slat cove is strongly three-dimensional and contains complex recirculating structures, some of which may also be responsible for the three-dimensional instability of the shed vortices originating from the slat cusp shear layer. This kind of three-dimensional flow physics is beyond the scope of the current two-dimensional measurements. However, figures 11–12 and 15–17 present the reconstructed velocity fields within the frequency bands related to narrowband peaks and therefore show the recirculating structures with two-dimensionality. This kind of two-dimensional recirculating structures plays an important role in the current hydrodynamic feedback and is expected to persist to $Re_c \sim 10^6$.

In summary, the strong evidence from the current work and in the literature have been discussed in this section to show that the vortex dynamics in the range of $2.41 \times 10^4 \leq Re_c \leq 5.2 \times 10^4$ can persist to the range of $Re_c \sim 10^6$. The feedback mechanisms at $Re_c \sim 10^4$ and $Re_c \sim 10^6$ are intrinsically similar and responsible for the narrowband peaks. However, these conclusions still need further verifications. Reliable time-resolved databases of the slat flows at $Re_c = 10^5$–10^6 should be pursued in future work to verify these conclusions.

6. Conclusions

Time-resolved particle image velocimetry measurements around the slat of a 30P30N multi-element airfoil are carried out within the range of $9.3 \times 10^3 \leq Re_c \leq 5.2 \times 10^4$ ($\alpha = 4\,^\circ$). The effects of Re_c on the mean flow topology and vortex dynamics around the slat are presented. Particularly, strong links between the frequency properties and the vortex shedding patterns of the slat cusp shear layer are evidently revealed in the current work. To the best of the authors' knowledge, such strong links have not been proposed before. Furthermore, the extension of the vortex dynamics at the current low Reynolds number to the range of $Re_c \sim 10^6$ is verified by in-depth discussions.

For the mean flow topology, the free shear layer originating from the slat cusp impinges on the underside of the slat trailing edge at $Re_c = 9.3 \times 10^3$. The main recirculation and the secondary counter-rotating recirculation lead to a double-recirculation pattern in the slat cove. As Re_c increases, the main recirculation shrinks in the streamwise direction and the impingement location of the slat cusp shear layer moves away from the trailing edge. Meanwhile, the double-recirculation pattern turns into a single-recirculation pattern when $Re_c \geq 4.61 \times 10^4$, owing to the disappearance of the secondary recirculation. At $Re_c = 5.2 \times 10^4$, the single-recirculation pattern and the estimated distance between the impingement location and the slat trailing edge are consistent with those at $Re_c \sim 10^6$.

For the vortex dynamics, a hydrodynamic feedback links the slat cusp and trailing edge when vortex shedding occurs to the slat cusp shear layer ($Re_c \geq 1.38 \times 10^4$). The shed vortices impinge on the underside of the slat trailing edge and generate fluctuations around the slat trailing edge. These fluctuations are convected to the slat cusp by the recirculation in the slat cove. The slat cusp shear layer will be disturbed by these fluctuations to generate new shed vortices. When $1.38 \times 10^4 \leq Re_c \leq 1.83 \times 10^4$, the formations and deformations of shed vortices lead to the dominance of fundamental frequency and harmonics in the slat cusp shear layer, respectively. The impingement locations of the shed vortices are steady on the underside of the trailing edge. As Re_c increases ($2.41 \times 10^4 \leq Re_c \leq 5.2 \times 10^4$), in addition to the fundamental frequency and harmonics, subharmonics and fractional harmonics occur to the slat cusp shear layer. The subharmonics make the impingement locations of the shed vortices unsteady on the underside of the trailing edge. The fractional harmonics can trigger the secondary instability of the braid region between two consecutive vortices to generate more shed vortices. More interestingly, mode switching occurs in the frequency properties of the slat cusp shear layer at $Re_c = 5.2 \times 10^4$, which is ascribed to the switching of vortex shedding patterns from one to another.

The vortex dynamics in the current range of $2.41 \times 10^4 \leq Re_c \leq 5.2 \times 10^4$ can persist to the range of $Re_c \sim 10^6$. The feedback mechanisms at $Re_c \sim 10^4$ and $Re_c \sim 10^6$ are intrinsically similar and responsible for the narrowband peaks. As a result, additional details on the production of slat noise at $Re_c \sim 10^6$ are provided. The impingement of large-scale shed vortices on the underside of the slat cove generates fluctuations around the slat trailing edge. As sound waves, these fluctuations can be convected to the slat cusp by the aeroacoustic feedback in the slat cove and be emitted to the far-fields for producing slat noise. The slat cusp shear layer will be disturbed by the fluctuations, which have been convected to the slat cusp, to generate vortices with different shedding patterns. The fluctuations with fundamental frequency trigger the fundamental shedding pattern of the slat cusp shear layer. The subharmonics in the slat cusp shear layer make the large-scale shed vortices impinge on the underside of the trailing edge with unsteady impingement locations. By triggering the secondary instability of the braid region, the fractional harmonics make the slat cusp shear layer generate more shed vortices than the fundamental frequency. Consequently, fluctuations produced by the impingement inherit the frequency properties pertaining to the different vortex shedding patterns of the slat cusp shear layer. As expected, the narrowband peaks (or tonal peaks) of the far-field slat noise at $Re_c \sim 10^6$ are the products of the fundamental frequency, harmonics, subharmonics and fractional harmonics in the slat cusp shear layer. The mode switching between the different vortex shedding patterns of the slat cusp shear layer leads to the mode switching between the different narrowband peaks of the far-field slat noise at $Re_c \sim 10^6$. It is hoped that the current conclusions will assist in the understanding of the vortex dynamics around the slat cove at $Re_c \sim 10^6$.

Reliable time-resolved databases of the slat flows at $Re_c = 10^5$–10^6 should be pursued in future work to further verify the conclusions of the current work. The surface pressure distributions on the airfoil should also be investigated in future work to estimate whether the present conclusions are insensitive to the effective angle of attack to a certain extent.

Acknowledgements. The authors thank Dr L. Li and Dr H. Guo for the many fruitful discussions regarding this work. The authors also thank the anonymous reviewers whose comments and suggestions greatly improved the quality and clarity of the manuscript.

Funding. The authors acknowledge the financial support of the National Natural Science Foundation of China (11721202).

Declaration of interests. The authors report no conflict of interest.

Author ORCIDs.
Jin-Jun Wang http://orcid.org/0000-0001-9523-7403.

References

Agoropoulos, D. & Squire, L. 1988 Interactions between turbulent wakes and boundary layers. *AIAA J.* **26** (10), 1194–1200.

Ashton, N., West, A. & Mendonça, F. 2016 Flow dynamics past a 30P30N three-element airfoil using improved delayed detached-eddy simulation. *AIAA J.* **54** (11), 3657–3667.

Boutilier, M.S.H. & Yarusevych, S. 2012 Effects of end plates and blockage on low-Reynolds-number flows over airfoils. *AIAA J.* **50** (7), 1547–1559.

Champagnat, F., Plyer, A., Le Besnerais, G., Leclaire, B., Davoust, S. & Le Sant, Y. 2011 Fast and accurate PIV computation using highly parallel iterative correlation maximization. *Exp. Fluids* **50** (4), 1169–1182.

Choudhari, M. & Lockard, D.P. 2015 Assessment of slat noise predictions for 30P30N high-lift configuration from BANC-III workshop. *AIAA Paper* 2015-2844.

Choudhari, M.M. & Khorrami, M.R. 2007 Effect of three-dimensional shear-layer structures on slat cove unsteadiness. *AIAA J.* **45** (9), 2174–2186.

Deck, S. & Laraufie, R. 2013 Numerical investigation of the flow dynamics past a three-element aerofoil. *J. Fluid Mech.* **732**, 401–444.

Dobrzynski, W. 2010 Almost 40 years of airframe noise research: what did we achieve? *J. Aircraft* **47** (2), 353–367.

Farge, M. 1992 Wavelet transforms and their applications to turbulence. *Annu. Rev. Fluid Mech.* **24** (1), 395–458.

Haller, G. 2001 Distinguished material surfaces and coherent structures in three-dimensional fluid flows. *Physica* D **149** (4), 248–277.

Haller, G. & Yuan, G. 2000 Lagrangian coherent structures and mixing in two-dimensional turbulence. *Physica* D **147** (3), 352–370.

He, G.-S., Pan, C., Feng, L.-H., Gao, Q. & Wang, J.-J. 2016 Evolution of Lagrangian coherent structures in a cylinder-wake disturbed flat plate boundary layer. *J. Fluid Mech.* **792**, 274–306.

Herr, M., Pott-Pollenske, M., Ewert, R., Boenke, D., Siebert, J., Delfs, J., Rudenko, A., Büscher, A., Friedel, H. & Mariotti, I. 2015 Large-scale studies on slat noise reduction. *AIAA Paper* 2015-3140.

Imamura, T., Ura, H., Yokokawa, Y. & Yamamoto, K. 2009 A far-field noise and near-field unsteadiness of a simplified high-lift-configuration model (slat). *AIAA Paper* 2009-1239.

Jawahar, H.K., Ali, S.A.S., Azarpeyvand, M. & da Silva, C.R.I. 2020 Aerodynamic and aeroacoustic performance of high-lift airfoil fitted with slat cove fillers. *J. Sound Vib.* **479**, 115347.

Jenkins, L.N., Khorrami, M.R. & Choudhari, M. 2004 Characterization of unsteady flow structures near leading-edge slat: part I. PIV measurements. *AIAA Paper* 2004-2801.

Kegerise, M.A., Spina, E.F., Garg, S. & Cattafesta III, L.N. 2004 Mode-switching and nonlinear effects in compressible flow over a cavity. *Phys. Fluids* **16** (3), 678–687.

Khorrami, M.R., Berkman, M.E. & Choudhari, M. 2000 Unsteady flow computations of a slat with a blunt trailing edge. *AIAA J.* **38** (11), 2050–2058.

Kolb, A., Faulhaber, P., Drobietz, R. & Grünewald, M. 2007 Aeroacoustic wind tunnel measurements on a 2D high-lift configuration. *AIAA Paper* 2007-3447.

LI, L., LIU, P.-Q., GUO, H., HOU, Y.-J., GENG, X. & WANG, J.-J. 2017 Aeroacoustic measurement of 30P30N high-lift configuration in the test section with Kevlar cloth and perforated plate. *Aerosp. Sci. Technol.* **70**, 590–599.

LI, L., LIU, P.-Q., XING, Y. & GUO, H. 2018*a* Time-frequency analysis of acoustic signals from a high-lift configuration with two wavelet functions. *Appl. Acoust.* **129**, 155–160.

LI, L., LIU, P., XING, Y. & GUO, H. 2018*b* Wavelet analysis of the far-field sound pressure signals generated from a high-lift configuration. *AIAA J.* **56** (1), 432–437.

LOCKARD, D. & CHOUDHARI, M. 2012 The influence of realistic Reynolds numbers on slat noise simulations. *AIAA Paper* 2012-2101.

MALLAT, S. 1999 *A Wavelet Tour of Signal Processing*. Elsevier.

MANOHA, E. & POTT-POLLENSKE, M. 2015 LEISA2: an experimental database for the validation of numerical predictions of slat unsteady flow and noise. *AIAA Paper* 2015-3137.

MORLET, J. 1983. Sampling theory and wave propagation. In *Issues in Acoustic Signal/Image Processing and Recognition* (ed. C.H. Chen), chap. 12, pp. 233–261. Springer.

MURAYAMA, M., NAKAKITA, K., YAMAMOTO, K., URA, H., ITO, Y. & CHOUDHARI, M.M. 2014 Experimental study of slat noise from 30P30N three-element high-lift airfoil in JAXA hard-wall low-speed wind tunnel. *AIAA Paper* 2014-2080.

OLSON, S., THOMAS, F.O. & NELSON, R.C. 2001 Mechanisms of slat noise production in a 2D multi-element airfoil configuration. *AIAA Paper* 2156-2156.

PAGANI, C.C. JR, SOUZA, D.S. & MEDEIROS, M.A. 2016 Slat noise: aeroacoustic beamforming in closed-section wind tunnel with numerical comparison. *AIAA J.* **54** (7), 2100–2115.

PAGANI, C.C., SOUZA, D.S. & MEDEIROS, M.A.F. 2017 Experimental investigation on the effect of slat geometrical configurations on aerodynamic noise. *J. Sound Vib.* **394**, 256–279.

PAN, C., XUE, D., XU, Y., WANG, J.-J. & WEI, R.-J. 2015 Evaluating the accuracy performance of Lucas–Kanade algorithm in the circumstance of PIV application. *Sci. China Phys. Mech. Astron.* **58** (10), 1–16.

PASCIONI, K., CATTAFESTA, L.N. & CHOUDHARI, M.M. 2014 An experimental investigation of the 30P30N multi-element high-lift airfoil. *AIAA Paper* 2014-3062.

PASCIONI, K.A. & CATTAFESTA, L.N. 2016 Aeroacoustic measurements of leading-edge slat noise. *AIAA Paper* 2016-2960.

PASCIONI, K.A. & CATTAFESTA, L.N. 2018*a* An aeroacoustic study of a leading-edge slat: beamforming and far field estimation using near field quantities. *J. Sound Vib.* **429**, 224–244.

PASCIONI, K.A. & CATTAFESTA, L.N. 2018*b* Unsteady characteristics of a slat-cove flow field. *Phys. Rev. Fluids* **3** (3), 034607.

POTT-POLLENSKE, M., DELFS, J. & REICHENBERGER, J. 2013 A testbed for large scale and high Reynolds number airframe noise research. *AIAA Paper* 2013-2260.

QU, Y., WANG, J.-J., FENG, L.-H. & HE, X. 2019 Effect of excitation frequency on flow characteristics around a square cylinder with a synthetic jet positioned at front surface. *J. Fluid Mech.* **880**, 764–798.

ROSSITER, J. 1964 Wind tunnel experiments on the flow over rectangular cavities at subsonic and transonic speeds. *Tech. Rep.* RM 3438. Aeronautical Research Council.

SHADDEN, S.C., DABIRI, J.O. & MARSDEN, J.E. 2006 Lagrangian analysis of fluid transport in empirical vortex ring flows. *Phys. Fluids* **18** (4), 047105.

SMYTH, W.D. 2003 Secondary Kelvin–Helmholtz instability in weakly stratified shear flow. *J. Fluid Mech.* **497**, 67–98.

SOUZA, D.S., RODRÍGUEZ, D., HIMENO, F.H.T. & MEDEIROS, M.A.F. 2019 Dynamics of the large-scale structures and associated noise emission in airfoil slats. *J. Fluid Mech.* **875**, 1004–1034.

SQUIRE, L. 1989 Interactions between wakes and boundary-layers. *Prog. Aerosp. Sci.* **26** (3), 261–288.

TERRACOL, M., MANOHA, E. & LEMOINE, B. 2015 Investigation of the unsteady flow and noise generation in a slat cove. *AIAA J.* **54** (2), 469–489.

VAN DAM, C. 2002 The aerodynamic design of multi-element high-lift systems for transport airplanes. *Prog. Aerosp. Sci.* **38** (2), 101–144.

WANG, J.-S., FENG, L.-H., WANG, J.-J. & LI, T. 2018 Görtler vortices in low-Reynolds-number flow over multi-element airfoil. *J. Fluid Mech.* **835**, 898–935.

WANG, J.-S., WANG, J.-J. & KIM, K.-C. 2019 Wake/shear layer interaction for low-Reynolds-number flow over multi-element airfoil. *Exp. Fluids* **60** (1), 1–24.

WELCH, P. 1967 The use of fast Fourier transform for the estimation of power spectra: a method based on time averaging over short, modified periodograms. *IEEE Trans. Audio Electroacoust.* **15** (2), 70–73.

ZHANG, Y.-F., CHEN, H.-X., WANG, K. & WANG, M. 2017 Aeroacoustic prediction of a multi-element airfoil using wall-modeled large-eddy simulation. *AIAA J.* **55** (12), 4219–4233.